PCCP

ROYAL SOCIETY OF CHEMISTRY

PAPER

View Article Online
View Journal | View Issue

Check for updates

Cite this: *Phys. Chem. Chem. Phys.*, 2023, **25**, 13593

Microhydration of the adamantane cation: intracluster proton transfer to solvent in $[Ad(H_2O)_{n=1-5}]^+$ for $n \geq 3$†

Martin Andreas Robert George and Otto Dopfer *

Received 3rd April 2023,
Accepted 26th April 2023

DOI: 10.1039/d3cp01514a

rsc.li/pccp

Radical cations of diamondoids are important intermediates in their functionalization reactions in polar solvents. To explore the role of the solvent at the molecular level, we characterize herein microhydrated radical cation clusters of the parent molecule of the diamondoid family, adamantane ($C_{10}H_{16}$, Ad), by infrared photodissociation (IRPD) spectroscopy of mass-selected $[Ad(H_2O)_{n=1-5}]^+$ clusters. IRPD spectra of the cation ground electronic state recorded in the CH/OH stretch and fingerprint ranges reveal the first steps of this fundamental H-substitution reaction at the molecular level. Analysis of size-dependent frequency shifts with dispersion-corrected density functional theory calculations (B3LYP-D3/cc-pVTZ) provides detailed information about the acidity of the proton of Ad^+ as a function of the degree of hydration, the structure of the hydration shell, and the strengths of the CH···O and OH···O hydrogen bonds (H-bonds) of the hydration network. For $n = 1$, H_2O strongly activates the acidic C–H bond of Ad^+ by acting as a proton acceptor in a strong CH···O ionic H-bond with cation-dipole configuration. For $n = 2$, the proton is almost equally shared between the adamantyl radical ($C_{10}H_{15}$, Ady) and the $(H_2O)_2$ dimer in a strong C···H···O ionic H-bond. For $n \geq 3$, the proton is completely transferred to the H-bonded hydration network. The threshold for this size-dependent intracluster proton transfer to solvent is consistent with the proton affinities of Ady and $(H_2O)_n$ and confirmed by collision-induced dissociation experiments. Comparison with other related microhydrated cations reveals that the acidity of the CH proton of Ad^+ is in the range of strongly acidic phenol$^+$ but lower than for cationic linear alkanes such as pentane$^+$. Significantly, the presented IRPD spectra of microhydrated Ad^+ provide the first spectroscopic molecular-level insight of the chemical reactivity and reaction mechanism of the important class of transient diamondoid radical cations in aqueous solution.

1. Introduction

Adamantane ($C_{10}H_{16}$, Ad) is the parent molecule of the diamondoid family, which is a fundamental class of sp^3-hybridized hydrocarbon molecules with diamond-like properties.[1–4] These H-passivated nanodiamonds are rigid and strain-free cycloalkanes with well-defined structures that are thermodynamically and chemically highly stable and perfectly size-selectable.[1–3] Due to their unique and largely variable properties, diamondoids and their derivatives are promising building blocks for new nanomaterials with tailored mechanical, electronic, optical, and chemical properties, with numerous applications in materials and polymer sciences, molecular electronics, biomedical sciences, and chemical synthesis.[5–14] Furthermore, their high stability suggests their occurrence in interstellar environments, which makes them highly relevant for astrochemistry.[15–20] For most applications, however, bare diamondoids must be functionalized to obtain the desired derivatives,[4] such as the amino-derivatives amantadine ($C_{10}H_{17}N$) or memantine ($C_{12}H_{21}N$), two drugs frequently used in various pharmaceutical applications.[9,21–26] In such functionalization reactions occurring in polar solvents, radical cations of diamondoids play an important role as reactive intermediates.[8,27,28] Quantum chemical calculations predict that solvation with polar ligands such as water or acetonitrile leads to significant activation and eventually rupture of the most acidic C–H bond of these radical cations, which corresponds to the initial step of H-substitution in these functionalization reactions (*e.g.*, single electron transfer oxidation).[8,27,28] Understanding the reaction mechanism at the molecular level requires detailed knowledge of the interaction between the diamondoid radical cation and the

---

Institut für Optik und Atomare Physik, Technische Universität Berlin, Hardenbergstr. 36, 10623 Berlin, Germany. E-mail: dopfer@physik.tu-berlin.de

† Electronic supplementary information (ESI) available. See DOI: **https://doi.org/10.1039/d3cp01514a**

surrounding solvent molecules. To this end, we analyse herein infrared photodissociation (IRPD) spectra of size-selected $[Ad(H_2O)_n]^+$ clusters with $n = 1–5$ generated in a molecular beam using quantum chemical dispersion-corrected density functional theory (DFT) calculations at the B3LYP-D3/cc-pVTZ level, with the major goal of characterizing the interaction between Ad^+ and water molecules and thus the first step of this prototypical functionalization reaction mechanism. This dual experimental and computational approach has proven successful in our laboratory in the study of a large variety of microhydrated cations and provides direct access to the interaction potential between the cation and solvent molecules.[29–39]

From the numerous studies performed on Ad and its cation, such as quantum chemical calculations,[8,27,40–42] IR and Raman spectroscopy,[43–46] photoelectron and fragmentation spectroscopy,[42,47–51] and IR and electronic photodissociation spectroscopy,[40,52] it is known that neutral Ad has a highly symmetric structure with T_d symmetry and a fully occupied triply degenerate $(7t_2)^6$ HOMO. This geometry becomes Jahn–Teller distorted upon ionization, leading to a $^2A_1$ cation ground electronic state with $(12e)^4(12a_1)^1$ configuration and C_{3v} symmetry. The removal of the bonding t_2 electron strongly stretches one of the C–H bonds along the C_3 axis, which has experimentally been quantified in IRPD spectra of $Ad^+(He)_n$ and $Ad^+(N_2)$ clusters based on its unusually low C–H stretch frequency at 2600 cm^{-1}.[40] In our previous IRPD study of monohydrated Ad^+,[30] we demonstrated further hydration-induced activation of this acidic C–H bond by forming a strong CH···O ionic H-bond in $Ad^+(H_2O)$. Despite this strong bonding, the H_2O ligand undergoes essentially free internal rotation due to the weak angular anisotropy of this intermolecular bond. Based on this previous study, we gradually increase herein the number of H_2O ligands to investigate successive microhydration of Ad^+ and to determine the critical cluster size n_c for intracluster proton transfer (ICPT) of the acidic proton of Ad^+ to the $(H_2O)_n$ solvent cluster. As the calculated proton affinity of the adamantyl radical (Ady, $C_{10}H_{15}$, PA = 868 kJ mol^{-1})[30] is in the range of the proton affinities of small $(H_2O)_n$ clusters (PA = 691, 808, 862, 900, 904, and 908 kJ mol^{-1} for $n = 1–6$),[53–57] we expect ICPT to occur at the cluster size of $n_c \approx 3$, *i.e.* within the size range considered herein ($n \leq 5$). This critical size range is also in line with previous computational predictions.[27] However, the critical size depends not only on the relative proton affinities but also on the solvation energies, the structures of the molecular ion and the $(H_2O)_n$ network within the cluster, the local charge distributions, and the way of generating the clusters. Comparing the ICPT with that observed for other microhydrated cations such as alkanes or polycyclic aromatic hydrocarbons (PAHs) provides a measure for the acidity and reactivity of the C–H bond in Ad^+. Furthermore, our analysis of the IRPD spectra of $[Ad(H_2O)_{n=1–5}]^+$ provides information on the strength of the OH···O H-bonds and the structure of the microhydration network. Significantly, these results represent the first experimental (and in particular spectroscopic) characterization of the first step of the fundamental H-substitution functionalization reaction mechanism at the molecular level for any diamondoid cation.

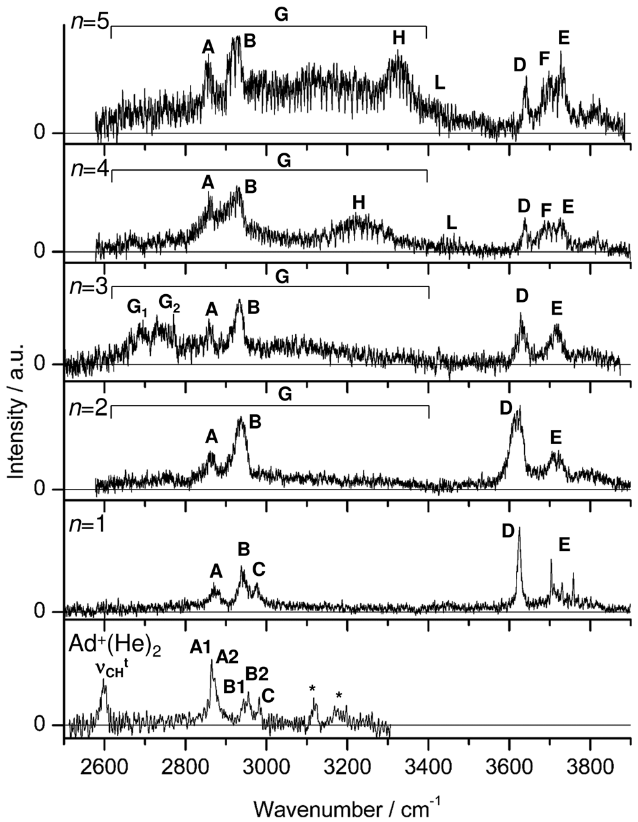

Fig. 1 IRPD spectra of $[Ad(H_2O)_{n=1–5}]^+$ in the 2500–3900 cm^{-1} range recorded in the H_2O loss channel compared to IRPD spectrum of $Ad^+(He)_2$.[40] The position, widths, and assignments of the transitions observed (A–H) are listed in Table 1.

2. Experimental and computational techniques

The IRPD spectra of mass-selected $[Ad(H_2O)_n]^+$ clusters ($n = 1–5$) shown in Fig. 1 are recorded in a tandem quadrupole mass spectrometer coupled to an electron ionization (EI) cluster ion source described elsewhere.[31,58] Briefly, cold cluster ions are produced in a pulsed supersonic plasma expansion by electron or chemical ionization of Ad and subsequent clustering reactions. The expansion gas is generated by passing a carrier gas (8 bar) through a reservoir containing solid Ad (Sigma-Aldrich, >99%, heated to 130 °C). Distilled H_2O is added into the gas line just before the sample reservoir to produce $[Ad(H_2O)_n]^+$ clusters. The $[Ad(H_2O)_n]^+$ parent clusters of interest are mass-selected by the first quadrupole and irradiated in the adjacent octupole by an IR laser pulse generated by an optical parametric oscillator pumped by a nanosecond Q-switched Nd:YAG laser. The IR radiation (ν_{IR}) is characterized by 10 Hz repetition rate, <1 cm^{-1} bandwidth, and pulse energies of 2–5 and 0.1–0.5 mJ in the XH stretch (XH = OH/CH, 2500–3900 cm^{-1}) and fingerprint ranges (800–2200 cm^{-1}), respectively. Calibration of the IR laser frequency to better than 1 cm^{-1} is achieved by a wavemeter. Resonant vibrational excitation upon single photon absorption leads to evaporation of a single H_2O ligand. The resulting fragments ions are selected by the second quadrupole and monitored as a function of ν_{IR} by a Daly ion detector to derive the IRPD spectra of $[Ad(H_2O)_n]^+$. To compensate for metastable decay, the ion source is triggered at twice the laser frequency and signals from alternate triggers are subtracted. All IRPD spectra are normalized for frequency-dependent variations in the photon flux. Collision-induced dissociation (CID) experiments are performed to confirm the chemical composition of the mass-selected $[Ad(H_2O)_n]^+$ clusters (Fig. S1 and S2, ESI†).

Quantum chemical calculations are performed at the dispersion-corrected B3LYP-D3/cc-pVTZ level (without Becke–Johnson damping) to determine the energetic, structural, electronic, and vibrational properties of Ad, Ad^+, and its $[Ad(H_2O)_n]^+$ clusters. As shown for $Ad^+(H_2O)$ and related clusters such as amantadine$^+(H_2O)_n$ and amantadineH$^+(H_2O)_n$, this computational level reproduces the experimental IR spectra and binding energies with satisfactory accuracy and represents an efficient compromise between accuracy and calculation time.[29,30,59] All structures shown in this work are confirmed as minima by harmonic frequency analysis. Relative energies (E_e) and binding energies (D_e) are corrected for harmonic zero-point vibrational energies to derive E_0 and D_0 values, respectively. Harmonic vibrational frequencies are scaled by a factor of 0.963 to optimize the agreement between calculated and measured OH stretch frequencies of H_2O (3657 and 3756 cm^{-1}).[60] Computed IR stick spectra are convoluted with Gaussian line profiles (fwhm = 10 cm^{-1}) to facilitate convenient comparison with the measured IRPD spectra. Natural bond orbital (NBO) analysis is employed to evaluate the charge distribution and charge transfer in $[Ad(H_2O)_n]^+$ as well as the second-order perturbation energies ($E^{(2)}$) of donor–acceptor orbital interactions involved in the H-bonds.[61,62] Cartesian coordinates, isomer-specific assignments to experimental values (Tables S1–S4, ESI†), energies (Tables S5–S9, ESI†), NBO charge distributions (Fig. S3–S6, ESI†) and calculated equilibrium structures with all binding parameters (Fig. S7–S11, ESI†) of all relevant structures are provided in the ESI.† Due to the large number of possible isomers, not all of them will be discussed in detail here. For completeness, their IR spectra may be found in the ESI† (Fig. S12–S19).

3. Experimental results

IRPD spectra of $[Ad(H_2O)_{n=1-5}]^+$ recorded in the CH/OH stretch range are compared in Fig. 1 to the previously analyzed spectrum of $Ad^+(He)_2$,[40] which closely resembles that of bare Ad^+. The positions, widths, and suggested vibrational assignments are listed in Table 1. The spectral range investigated (2500–3900 cm^{-1}) covers aliphatic CH stretch modes (A–C, ν_{CH_n}, 2500–3000 cm^{-1}) and both free (D, E, F, $\nu_{OH}^{f/a/s}$, 3600–3800 cm^{-1}) and bound OH stretch modes (G, H, L, $\nu_{OH}^{b}/\nu_{OH}^{b\text{-ring}}$, 2700–3500 cm^{-1}) of the (protonated) H_2O ligands. Compared to the $Ad^+(He)_2$ spectrum, the intense ν_{CH}^{t} transition characteristic of the acidic C–H bond of bare Ad^+ located on its C_3 axis is absent in the spectra of $[Ad(H_2O)_{n=1-5}]^+$, indicating that in all observed microhydrated clusters this acidic C–H bond is hydrated. Similarly, the $Ad^+(He)_2$ bands between 3100 and 3200 cm^{-1} marked by asterisks in Fig. 1 and previously attributed to overtone or combinations bands,[40] disappear in the $[Ad(H_2O)_{n=1-5}]^+$ spectra, because of the significant impact of hydration on the Ad^+ cage. The remaining CH stretch bands A (2868/2883 cm^{-1}), B (2941/2954 cm^{-1}), and C (2981 cm^{-1}) of $Ad^+(He)_2$ are present in the $n = 1$ spectrum with similar frequencies (2875, 2942, 2976 cm^{-1}), while only bands A and B are observed in the $n > 1$ spectra, with slight redshifts to ∼2860 and ∼2935 cm^{-1}, respectively. This observation indicates a change in the Ad^+ cage structure for $n \geq 2$, possibly a first indication of approaching the structure of neutral Ady due to incident ICPT. The symmetric and antisymmetric free OH stretch bands D and E of the H_2O ligands appear at 3625 ($n = 1$) to 3642 cm^{-1} ($n = 5$) and 3717 ($n = 1$) to 3727 cm^{-1} ($n = 5$), respectively. Compared to bare H_2O ($\nu_{OH}^{s/a}$ = 3657/3756 cm^{-1}),[63]

Table 1 Positions (in cm^{-1}), widths (fwhm in parenthesis) and vibrational assignments of the transitions observed in the IRPD spectra of $[Ad(H_2O)_n]^+$ and $Ad^+(He)_2$ recorded in the XH stretch and fingerprint ranges (Fig. 1 and 10)

Peak	Mode[a]	$Ad^+(He)_2$[b]	$[Ad(H_2O)]^{+}$[c]	$[Ad(H_2O)_2]^+$	$[Ad(H_2O)_3]^+$	$[Ad(H_2O)_4]^+$	$[Ad(H_2O)_5]^+$
I	β_{CH_2}		1461 (25)				
J	β_{OH_2}		1633 (18)				
K	$\nu_{CH\cdots O}/\nu_{OH\cdots C}$		≥2200	≤1100	≥1500		
	ν_{CH}^{t}	2600					
G	ν_{OH}^{b}			2600–3400	2600–3400	2600–3400	2600–3400
G_1					2695 (17)		
G_2					2751 (36)		
A	ν_{CH_n}	2868 A1 2883 A2	2875 (23)	2863 (19)	2858 (14)	2861 (14)	2857 (15)
B	ν_{CH_n}	2941 B1 2954 B2	2942 (20)	2937 (30)	2934 (19)	2927 (33)	2926 (23)
C	ν_{CH_n}	2981	2976 (13)				
H	ν_{OH}^{b}					3220 (68)	3323 (58)
L	$\nu_{OH}^{b\text{-ring}}$					3430–3480	3415 (15)
D	$\nu_{OH}^{s}/\nu_{OH}^{f}$		3625 (13)	3626 (23)	3628 (20)	3639 (14)	3642 (12)
F	ν_{OH}^{f}					3692 (14)	3690 (14)
E	ν_{OH}^{a}		3703–3759[d]	3721 (18)	3718 (24)	3726 (16)	3727 (22)

[a] Stretching (ν), bending (β). [b] Ref. 36. [c] Ref. 26. [d] Band origin at 3717 cm^{-1}.

these bands are redshifted by 32 and 39 cm^{-1} for Ad$^+$(H_2O), respectively, indicative of a strongly bound cation-dipole structure.[30] As a special feature, the n = 1 spectrum shows rotationally resolved substructure for band E (ν_{OH}^{a}), with narrow and nearly equidistant Q branches at 3703, 3731, and 3759 cm^{-1}. These arise from nearly free internal rotation of the H_2O ligand, as discussed in detail in our recent report.[30] For n > 3 additional well-resolved bands (F) are observed in the free OH stretch range at ~3700 cm^{-1}, which can be attributed to free and uncoupled ν_{OH}^{f} modes of H_2O ligands in a H-bonded solvent network. Interestingly, a broad background signal (G) between 2600 and 3400 cm^{-1} appears in the n = 2 spectrum, which is not present in the n = 1 spectrum and assigned to a strongly redshifted ν_{OH}^{b} mode of a proton donor in a OH···O H-bond of a $(H_2O)_2$ attached to Ad$^+$. In this scenario, the ν_{OH}^{b} frequency is drastically reduced compared to that of bare $(H_2O)_2$ at 3601 cm^{-1},[64,65] indicative of an unusually strong OH···O H-bond. Such a strong H-bond is difficult to rationalize only by large cooperativity of a neutral H-bonded $(H_2O)_2$ dimer, suggesting that partial charge is transferred to the H_2O ligands due to the onset of ICPT within the cluster. This assignment also explains the large width of the transition, which is typical for proton-donor stretch modes.[66–71] In addition, transition D in the n = 2 spectrum is more intense and broader (23 cm^{-1}) than in the other spectra, which may be an indication of a ν_{OH}^{f} mode overlapping with the ν_{OH}^{s} transition, which is then the corresponding counterpart of the broad ν_{OH}^{b} mode. For n > 2, this background signal G becomes more and more intense, supporting the assignment to ν_{OH}^{b} mode(s) by comparison to IRPD spectra of related microhydrated clusters with proton-transferred structures.[66,69,70] Due to the large width of these transitions, a determination of a clear maximum is not possible for n = 2, 4, and 5, while in the n = 3 spectrum two maxima G_1 and G_2 can be identified at 2695 and 2751 cm^{-1}, respectively, which are probably due to ν_{OH}^{b} transitions with a larger redshift (below the free C–H stretch range) and simultaneous increase in IR intensity. In the n = 4 spectrum, the peak of band G can be located around ~2900 cm^{-1} due to the strong increase in signal between bands A and B. On the other hand, for n = 5 the maximum of this peak may be around ~3100 cm^{-1}, indicating a blueshift of the ν_{OH}^{b} mode(s) from n = 3 to n = 5. From n > 3 onwards, a broad transition H at 3220 cm^{-1} becomes evident, which clearly can be assigned to a ν_{OH}^{b} mode typical for a H-bonded network with medium-strength OH···O H-bonds. Between 3430 and 3480 cm^{-1}, a weak unresolved signal L is present in the range of $\nu_{OH}^{b\text{-ring}}$ modes of cyclic H-bonded water network structures. For n = 5, band H is narrower and blueshifted by 103 cm^{-1} to 3323 cm^{-1} (compared to n = 4) while band L is more distinct, intense, and slightly redshifted to 3415 cm^{-1}. Finally, all IRPD spectra reveal a band at 3800 cm^{-1}, which cannot be assigned to any fundamental. In addition to IRPD spectra in the XH stretch range, IRPD spectra of $[Ad(H_2O)_{n=1-3}]^+$ are measured in the fingerprint range. They are discussed separately in Section 5 due to their less informative value arising from reduced signal-to-noise ratio and spectral resolution.

The CID mass spectra of size-selected $[Ad(H_2O)_{n=1,2,6}]^+$ clusters show only the loss of H_2O ligands in the higher mass range (m/z > 120), so that mass contamination can be excluded (Fig. S1, ESI†). However, the CID spectrum of $[Ad(H_2O)_3]^+$ shows the additional loss of the Ady radical, producing the $H_7O_3^+$ ion with m/z 55 as a minor channel. Significantly, essentially no Ady loss is detected in the CID spectrum of n = 2 (Fig. S2, ESI†), providing a further indication for the threshold for ICPT at a critical size of n_c = 3.

4. Computational results and assignments

To determine possible structures giving rise to the measured IRPD spectra of $[Ad(H_2O)_{n\leq 5}]^+$, we consider the results of the quantum chemical calculations.

4.1. Ad$^{(+)}$ and H_2O monomers

The structures calculated for Ad, Ad$^+$, and H_2O shown in Fig. 2 agree well with available computational and experimental data.[8,27,40–42,53,60,63,72] Neutral Ad ($^1A_1$, T_d) has a highly

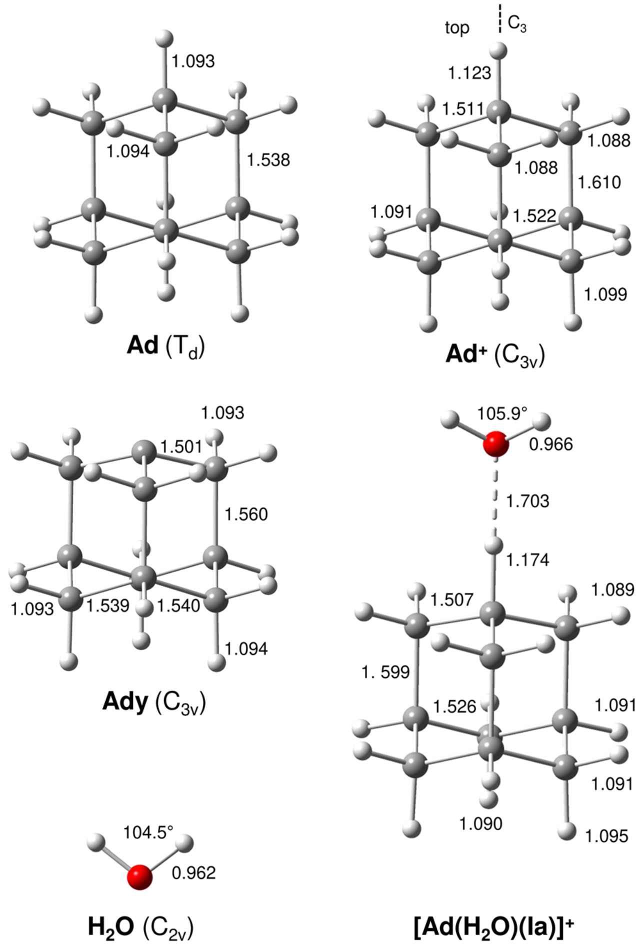

Fig. 2 Calculated equilibrium structures (in Å and degrees) of H_2O, Ad, Ad$^+$, Ady, and $[Ad(H_2O)(Ia)]^+$ in their ground electronic state (B3LYP-D3/cc-pVTZ).

symmetric tetrahedral cage structure with C–C and C–H bond lengths of 1.538 and 1.093/4 Å, respectively. Ionization of Ad into the electronic ground state of its cation results from the removal of a bonding electron from the t_2 orbital, leading to Jahn–Teller distortion in the resulting $^2A_1$ state with C_{3v} symmetry. In line with the a_1 HOMO (Fig. S20, ESI†), the main structural effects of ionization are an elongation of the three C–C bonds parallel to the C_3 axis by 72 mÅ (the other C–C bonds shrink by 27 and 16 mÅ) and a drastic elongation of the C–H bond lying on the C_3 axis by 30 mÅ (from 1.093 to 1.123 Å). Significantly, this apical C–H bond of Ad^+ becomes very acidic and carries the largest positive partial charge of all protons (354 m*e*, Fig. S3, ESI†), making it an attractive binding site for the H_2O ligands. As a result, its computed stretch frequency (ν_{CH}^{t}) shifts down from 2916 to 2606 cm^{-1}, in good agreement with experiment (2600 cm^{-1}, Fig. 1).[40]

4.2. $[Ad(H_2O)]^+$

Similar to Ad^+, $Ad^+(H_2O)$ has already been studied by IRPD and is therefore only briefly discussed here for completeness.[30] The IRPD spectrum is compared with the calculated IR spectra of the lowest-energy isomer $[Ad(H_2O)(Ia)]^+$ and H_2O in Fig. 3, and with the $[Ad(H_2O)(I–III)]^+$ isomers in Fig. S12 (ESI†). The corresponding structures are shown in Fig. 2 and Fig. S7, S8 (ESI†), and the vibrational assignments and relative energies are listed in Tables S1 and S5 (ESI†).

Briefly, the Jahn–Teller distorted Ad^+ cation offers three attractive binding sites for H_2O (top, bottom, side), but experimentally only the global minimum $[Ad(H_2O)(I)]^+$ represented by the averaged structure of two nearly isoenergetic minima $[Ad(H_2O)(Ia/Ib)]^+$ with $E_0 = 0$ and 0.26 kJ mol^{-1} (and a potential barrier of only 0.4 kJ mol^{-1} between them) is observed.[30] Here, H_2O binds with one of its lone pairs to the single acidic CH group of Ad^+ in a strong, short, and nearly linear CH···O ionic H-bond (1.70 Å, $\phi_{CHO} = 170.2°$), with favourable cation-dipole orientation and a calculated binding energy of $D_0 = 45$ kJ mol^{-1}. As a result of the strong CH···O H-bond, the corresponding intense ν_{CH}^{t} frequency is largely reduced from that of Ad^+ (2600 cm^{-1}) and shifts out of the range considered in Fig. 1 and 3 down to ~2000 cm^{-1} (Section 5). The remaining CH stretch bands A–C (2875, 2942, 2976 cm^{-1}) show only minor shifts upon monohydration. The new transitions D and E at 3625 and 3717 cm^{-1} arise from the $\nu_{OH}^{a/s}$ modes of H_2O slightly redshifted from those of bare H_2O (by 32/39 cm^{-1}), as is typical for cation-H_2O clusters.[29,35–37,73,74] Interestingly, the ν_{OH}^{a} band (E) of $Ad^+(H_2O)$ shows rotational fine structure with three narrow Q branches separated by 28 cm^{-1}, indicating nearly free internal H_2O rotation with an effective internal rotation constant of $A_{eff} = 14$ cm^{-1}.[30] The flat $Ad^+···H_2O$ potential near the global minimum causes fluxional bonding with low angular anisotropy. Significantly, monohydration leads to a further elongation of the acidic C–H bond (to 1.174 Å), which has been already activated by ionization of Ad (1.093 → 1.123 Å), resulting in a strong redshift of ν_{CH}^{t} down to 2033 cm^{-1}. Due to the disparity in the ionization energies of Ad and H_2O (9.25 *vs.* 12.6 eV),[60] charge transfer from Ad^+ to H_2O is limited and amounts to 124 m*e*. Moreover, due to the substantially higher proton affinity of Ady as compared to that of H_2O (PA = 868 *vs.* 691 kJ mol^{-1}),[30,53] monohydration is also not sufficient to induce proton transfer from Ad^+ to H_2O. Finally, the higher-energy isomers $[Ad(H_2O)(II,III)]^+$ ($E_0 = 3.5$ and 6.3 kJ mol^{-1}) with bonding of H_2O to the bottom and side of the Ad^+ cage are not observed because their intense and hardly shifted ν_{CH}^{t} bands near 2600 cm^{-1} are not detected.[30]

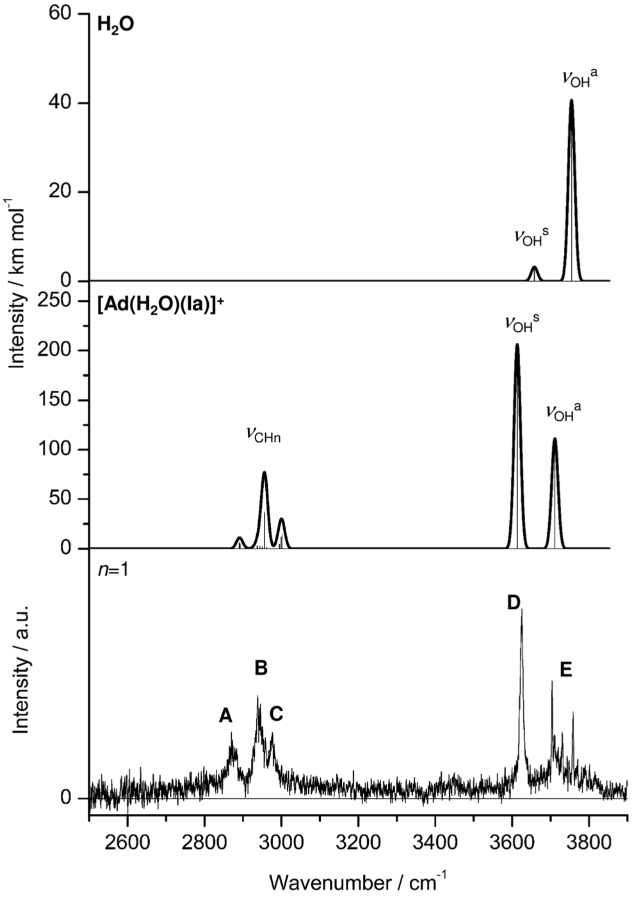

Fig. 3 IRPD spectrum of $[Ad(H_2O)]^+$ compared to linear IR absorption spectra of $[Ad(H_2O)(Ia)]^+$ and H_2O calculated at the B3LYP-D3/cc-pVTZ level. The positions of the transitions observed in the IRPD spectrum of $[Ad(H_2O)]^+$ and their vibrational assignment are listed in Table S1 (ESI†).

4.3. $[Ad(H_2O)_2]^+$

Seven isomers are found for $[Ad(H_2O)_2]^+$ (Fig. S13 and Table S6, ESI†). In the following, only the four lowest-energy isomers $[Ad(H_2O)_2(I–IV)]^+$ are discussed in more detail (Fig. 4, 5 and Fig. S9, ESI†), because the less favorable isomers ($E_0 >$ 25 kJ mol^{-1}) are not required for explaining the IRPD spectrum. For brevity, the structures and IR spectra of isomers II–IV are discussed only briefly herein and further details are provided in the ESI.†

The $[Ad(H_2O)_2(I)]^+$ global minimum ($E_0 = 0$) is formed by adding a second H_2O ligand to the first H_2O ligand of $[Ad(H_2O)(I)]^+$, resulting in a drastic further elongation of the apical C–H bond of Ad^+ (by 129 mÅ to 1.303 Å). This trend can

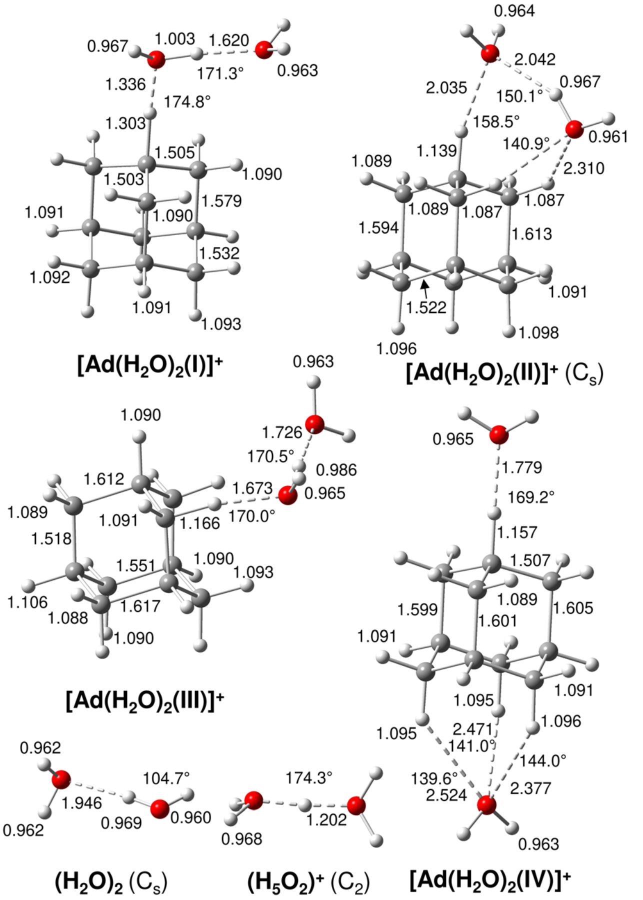

Fig. 4 Calculated equilibrium structures (in Å and degrees) of $(H_2O)_2$, $(H_5O_2)^+$, and $[Ad(H_2O)_2(I–IV)]^+$ in their ground electronic state (B3LYP-D3/cc-pVTZ). All bond lengths are shown in Fig. S9 (ESI†).

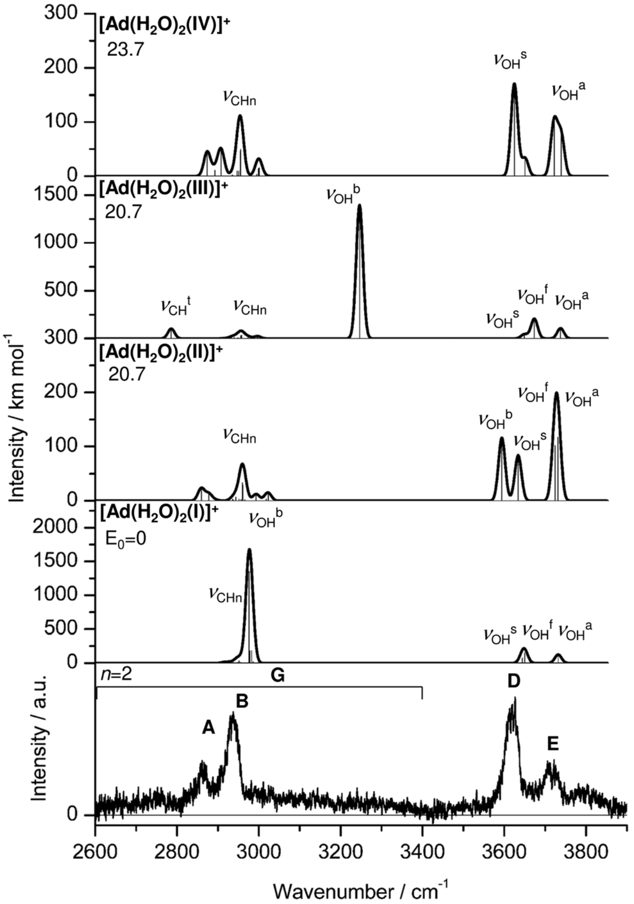

Fig. 5 IRPD spectrum of $[Ad(H_2O)_2]^+$ compared to linear IR absorption spectra of $[Ad(H_2O)_2(I–IV)]^+$ calculated at the B3LYP-D3/cc-pVTZ level. Note the different IR intensity scales for the computed IR spectra. The positions of the transition observed in the IRPD spectrum of $[Ad(H_2O)_2]^+$ and their vibrational assignment are listed in Table S2 (ESI†). Differences in relative energy (E_0) are given in kJ mol^{-1}.

be rationalized by the increased proton affinity of $(H_2O)_2$ compared to that of H_2O (PA = 808 *vs.* 691 kJ mol^{-1}),[53,54] and the strong cooperative effect of forming a H-bonded hydration network. In the strong and nearly linear C···H···O ionic H-bond (174.8°), the central proton is roughly midway between C and O (r_{CH} = 1.303 Å, r_{OH} = 1.336 Å). According to these bond distances, the proton is equally shared between Ady and $(H_2O)_2$. The dissociation energies for loss of $(H_2O)_2$ and Ady are calculated as D_0 = 86.3 and 123.4 kJ mol^{-1}, consistent with the corresponding PA values. The NBO analysis suggests almost complete proton transfer from Ad^+ to $(H_2O)_2$, because of the corresponding σ-type bonding orbital between the proton and O (Fig. S21, ESI†) with occupancy of 0.94. Moreover, the donor–acceptor interaction energy between the lone pair of C and the antibonding σ* orbital of the O–H donor bond is very high ($E^{(2)}$ = 220.54 kJ mol^{-1}), which explains the massive redshift of the former ν_{CH}^{t} mode of Ad^+ down to 818 cm^{-1}. Depending on whether the proton is assigned to the Ady cage or $(H_2O)_2$, this shared proton stretch (denoted $\nu_{C\cdots H\cdots O}$) may be considered either as a strongly redshifted $\nu_{CH\cdots O}$ mode of Ad^+ ($\Delta\nu_{CH}$ = 1788 cm^{-1}) or, as suggested by the NBO analysis, an even more strongly redshifted $\nu_{OH\cdots C}$ mode of $H_5O_2^+$ ($\Delta\nu_{OH}$ = 2772 cm^{-1}). These frequency shifts correspond to elongations of the C–H and O–H donor bonds of Δr_{CH} = 180 mÅ and Δr_{OH} = 368 mÅ (compared to H_3O^+, the values are $\Delta\nu_{OH}$ = 2616 cm^{-1} and Δr_{OH} = 356 mÅ). The charge transfer to the water ligands is increased to 274 m*e* for $(H_2O)_2$ or 697 m*e* for $H_5O_2^+$ (Fig. S4, ESI†). The OH···O H-bond in $[Ad(H_2O)_2(I)]^+$ is much stronger and shorter than in bare $(H_2O)_2$ ($r_{OH\cdots O}$ = 1.620 *vs.* 1.946 Å, $E^{(2)}$ = 58.9 *vs.* 16.9 kJ mol^{-1}), because of the strong cooperativity of the three-body polarization forces caused by the nearby positive charge. The O–H donor bond is stretched by 37 mÅ to 1.003 Å and the remaining free O–H bond is slightly elongated to 0.967 Å compared to $[Ad(H_2O)(Ia)]^+$. As a result, the corresponding ν_{OH}^{b} mode is redshifted down to 2976 cm^{-1}, consistent with an increase in IR intensity (factor ∼8), while the other ν_{OH} modes are slightly blueshifted to ν_{OH}^{f} = 3650, ν_{OH}^{s} = 3645, and ν_{OH}^{a} = 3732 cm^{-1}. The additional H_2O ligand causes the C–C bonds, stretched parallel to the C_3 axis by the Jahn–Teller distortion and shortened again by monohydration, to contract further by up to 21 mÅ to 1.579 and 1.581 Å, while the other C–C and C–H bonds are hardly affected by the addition of $(H_2O)_2$ to Ad^+ (Δr_{CC} < 6 mÅ, Δr_{CH} < 2 mÅ).

There is a large energy gap of E_0 = 20.7 kJ mol^{-1} between the global minimum I of n = 2 and the next stable isomers II–IV. In isomer II, one H_2O is bound to the acidic C–H donor of Ad^+ (CH$\cdots$O) and the second H_2O is attached to the adjacent CH_2 groups *via* weak CH$\cdots$O contacts. The two ligands are linked together by a very weak OH$\cdots$O H-bond ($E^{(2)}$ = 8.6 kJ mol^{-1}) and the CH$\cdots$O H-bond of the first H_2O to the acidic C–H group is much weaker and less linear (2.035 Å, 158.5°) than in isomer I, resulting in a smaller redshift of $\nu_{\mathrm{CH}}^{\mathrm{t}}$ to 2416 cm^{-1} and an only slightly redshifted $\nu_{\mathrm{OH}}^{\mathrm{b}}$ mode at 3594 cm^{-1}.

In isomer III (E_0 = 20.7 kJ mol^{-1}), a H-bonded $(H_2O)_2$ dimer is attached to a CH_2 group at the bottom of Ad^+ *via* a single CH$\cdots$O ionic H-bond ($D_0(H_4O_2)$ = 65.7 kJ mol^{-1}, $r_{\mathrm{CH\cdots O}}$ = 1.673 Å, ϕ_{CHO} = 170.0°, Δq = 179 me, $E^{(2)}$ = 101.4 kJ mol^{-1}), resulting in a massively redshifted $\nu_{\mathrm{CH}}^{\mathrm{b}}$ mode at 1984 cm^{-1}. The OH$\cdots$O H-bond of $(H_2O)_2$ is weaker, longer, and less linear compared to isomer I ($r_{\mathrm{OH\cdots O}}$ = 1.726, ϕ_{OHO} = 170.5°, $E^{(2)}$ = 36.6 kJ mol^{-1}), resulting in $\nu_{\mathrm{OH}}^{\mathrm{b}}$ = 3246 cm^{-1} and $\nu_{\mathrm{OH}}^{\mathrm{f}}$ = 3673 cm^{-1}.

In isomer IV (E_0 = 23.7 kJ mol^{-1}, $D_0(2H_2O)$ = 82.4 kJ mol^{-1}), one H_2O is bound to the acidic C–H bond of Ad^+ like in $[Ad(H_2O)(I)]^+$, while the other H_2O is attached to the three CH_2 groups at the bottom of Ad^+ *via* weak CH$\cdots$O contacts (2.377, 2.471, 2.524 Å, 139.6°, 141.0°, 144.0°), much like in $[Ad(H_2O)(III)]^+$. This leads to minor redshifts of the associated $\nu_{\mathrm{CH_2}}$ modes to 2874, 2892, and 2907 cm^{-1}. The CH$\cdots$O H-bond is weaker compared to $[Ad(H_2O)(Ia)]^+$ due to the additional H_2O at the bottom of Ad^+ ($r_{\mathrm{CH\cdots O}}$ = 1.703 *vs.* 1.779 Å, ϕ_{CHO} = 170.2° *vs.* 169.2°) leading to a smaller redshift of $\nu_{\mathrm{CH}}^{\mathrm{t}}$ (2033 *vs.* 2188 cm^{-1}).

Comparison of the measured IRPD spectrum of $[Ad(H_2O)_2]^+$ with the IR spectra computed for $[Ad(H_2O)_2(\text{I–IV})]^+$ in Fig. 5 demonstrates good agreement for the global minimum $[Ad(H_2O)_2(I)]^+$, with respect to the observed narrow bands A, B, D, and E (Table S2, ESI†). Bands A (2863 cm^{-1}) and B (2937 cm^{-1}) are assigned to ν_{CH_n} modes of isomer I and the $\nu_{\mathrm{OH}}^{\mathrm{s}}$ (3645 cm^{-1}) and $\nu_{\mathrm{OH}}^{\mathrm{a}}$ (3732 cm^{-1}) modes agree well with bands D (3626 cm^{-1}) and E (3721 cm^{-1}), respectively. The $\nu_{\mathrm{OH}}^{\mathrm{f}}$ mode (3650 cm^{-1}) is also attributed to band D (3626 cm^{-1}), which agrees well with its increase in width and intensity. Moreover, the IR spectrum of isomer I explains the disappearance of band C observed for n = 1 and n = 0. In contrast to the other isomers II–IV, in isomer I the C–H bonds of the CH_2 groups at the top of Ad^+ elongate to 1.090 Å and approach those of Ady (r_{CH} = 1.093 Å). The associated $\nu_{\mathrm{CH_2}}$ modes thus are redshifted similar to those of Ady (Fig. S22, ESI†) and can be assigned to peak B, which also explains the slight increase in intensity and width of this band. The intense redshifted $\nu_{\mathrm{OH}}^{\mathrm{b}}$ mode of isomer I at 2976 cm^{-1} is attributed to the broad background G, although no exact evaluation of its experimental frequency is possible due to the lack of a clear band maximum.

Despite its high energy difference of 20.7 kJ mol^{-1} to the global minimum, minor contributions of $[Ad(H_2O)_2(II)]^+$ cannot be ruled out completely. For example, the convoluted peaks of its ν_{CH_n} modes (2861 and 2958 cm^{-1}) agree with bands A (2863 cm^{-1}) and B (2937 cm^{-1}), and its only slightly redshifted $\nu_{\mathrm{OH}}^{\mathrm{b}}$ mode (3594 cm^{-1}) of the very weak OH$\cdots$O H-bond and $\nu_{\mathrm{OH}}^{\mathrm{f}}$ (3724 cm^{-1}) may contribute to bands D and E, respectively. On the other hand, the weaker convoluted peaks of the ν_{CH_n} modes at 2994 and 3021 cm^{-1} are not clearly discernible in the IRPD spectrum, but may contribute to the slight increase in signal at ~3000 cm^{-1}. As isomer II cannot account for the (integrated) background G, the population of isomer II is concluded to be small. A larger population of isomer III is also unlikely. Although the intense $\nu_{\mathrm{OH}}^{\mathrm{b}}$ mode (3246 cm^{-1}) may contribute to the background G and the blueshifted $\nu_{\mathrm{CH}}^{\mathrm{t}}$ mode (2786 cm^{-1}) may be assigned to the slightly elevated signal at ~2750 cm^{-1}, one would expect that with a significant population of III both the only slightly redshifted $\nu_{\mathrm{OH}}^{\mathrm{b}}$ mode and $\nu_{\mathrm{CH}}^{\mathrm{t}}$ would be detectable as more intense peaks. Isomer IV cannot be fully excluded either, because its ν_{CH_n} modes (2874 and 2955 cm^{-1}) are compatible with bands A (2863 cm^{-1}) and B (2937 cm^{-1}), and its ν_{OH} modes (3625, 3651, 3722, and 3739 cm^{-1}) agree with bands D (3626 cm^{-1}) and E (3721 cm^{-1}). The additional ν_{CH_n} mode of IV at 2907 cm^{-1} may be absorbed in band A and the convoluted peak of the ν_{CH_n} modes at 3000 cm^{-1} may produce the weak signal at ~3000 cm^{-1} (similar to the potential assignment of II). In conclusion, the by far most stable isomer I can explain all bands in the observed IRPD spectrum of the n = 2 cluster and thus is the favored assignment. Moreover, there is no clear indication for the presence of the energetically higher isomers II–IV, although minor contributions cannot be completely ruled out.

4.4. $[Ad(H_2O)_3]^+$

From the 13 computed isomers of $[Ad(H_2O)_3]^+$ (Fig. 6 and Fig. S14, Table S7, ESI†), we consider only the five most stable isomers below $E_0 < 20$ kJ mol^{-1} (Fig. 6, 7 and Fig. S10, ESI†). Moreover, isomers II–IV are discussed only briefly and more details are given in the ESI.† Isomers I–IV are all formed by H_2O attachment to the existing $(H_2O)_2$ chain of $[Ad(H_2O)_2(I)]^+$, while isomer V is derived from adding H_2O to the solvent chain of $[Ad(H_2O)_2(III)]^+$. All low-energy n = 3 isomers exhibit ICPT from Ad^+ to $(H_2O)_3$, consistent with the PA of Ady (868 kJ mol^{-1}) and the increasing PA of $(H_2O)_n$ clusters (808, 862, 900 kJ mol^{-1} for n = 2–4).[53–57]

In the $[Ad(H_2O)_3(I)]^+$ global minimum, the three protons of the hydronium ion (H_3O^+) are fully solvated by two H_2O molecules and the Ady radical, leading to an Eigen-type configuration. The linear OH$\cdots$C H-bond (ϕ_{CHO} = 180°) is characterized by a bond length of 1.626 Å, $D_0(H_7O_3{}^+)$ = 93.5 kJ mol^{-1}, and $E^{(2)}$ = 43.7 kJ mol^{-1} for the donor–acceptor orbital interaction between the lone pair of C and the antibonding σ* orbital of the O–H donor bond. ICPT increases the partial charge on the solvent molecules $(H_7O_3{}^+)$ to 875 me, leaving only a minor partial charge of 125 me on Ady (Fig. S5, ESI†). The bond length between the proton and O contracts drastically by 268 mÅ to 1.068 Å compared to $[Ad(H_2O)_2(I)]^+$. However, this newly formed chemical O–H bond is still much longer than in bare H_3O^+ or $H_7O_3{}^+$ (r_{OH} = 0.980 or 0.967 Å) due to its OH$\cdots$C H-bond to Ady. As a result, $\nu_{\mathrm{OH\cdots C}}$ ($\nu_{\mathrm{OH}}^{\mathrm{b}}$ = 1953 cm^{-1}) is strongly redshifted compared to $\nu_{\mathrm{OH}}^{\mathrm{f}}$ of bare

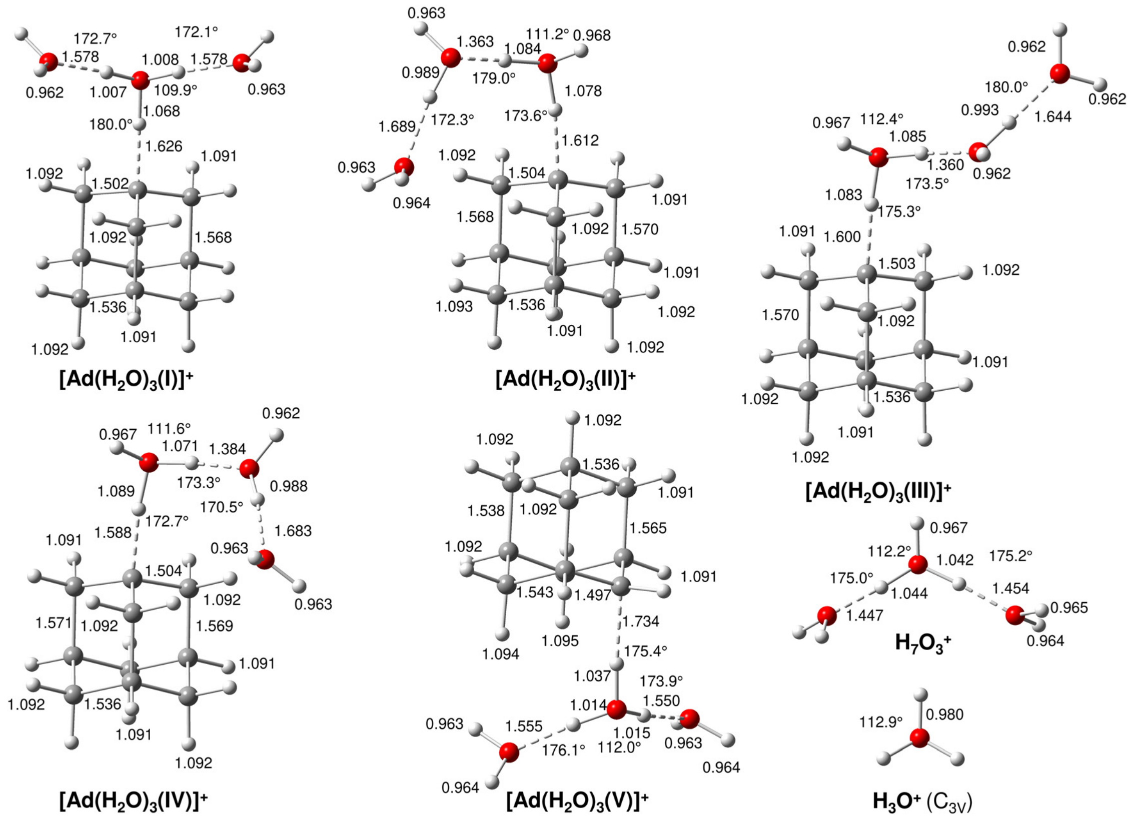

Fig. 6 Calculated equilibrium structures (in Å and degrees) of H_3O^+, $H_7O_3^+$ and $[Ad(H_2O)_3(I–V)]^+$ in their ground electronic state (B3LYP-D3/cc-pVTZ). All bond lengths are shown in Fig. S10 (ESI†).

$H_7O_3^+/H_3O^+$ (3656/3434 cm^{-1}). On the other hand, there is a large blueshift of 1135 cm^{-1} compared to the former $\nu_{C\cdots H\cdots O}$ mode of $[Ad(H_2O)_2(I)]^+$ at 818 cm^{-1}. The OH···O H-bonds are stronger, shorter, and more linear than in $[Ad(H_2O)_2(I)]^+$ ($r_{OH\cdots O}$ = 1.578 *vs.* 1.620 Å, ϕ_{OHO} = 172.7°/172.1° *vs.* 171.3°, $E^{(2)}$ = 70.0/68.8 *vs.* 58.9 kJ mol^{-1}), but longer, weaker, and less linear than in bare $H_7O_3^+$ ($r_{OH\cdots O}$ = 1.447/1.454 Å, ϕ_{OHO} = 175.0°/175.2°). The O–H proton donor bonds are slightly more stretched to 1.008/1.007 Å compared to $[Ad(H_2O)_2(I)]^+$), resulting in a redshift (96/45 cm^{-1}) of the corresponding coupled ν_{OH}^{b} modes (2880 and 2931 cm^{-1}). The terminal H_2O ligands have bond angles of 107.0° and bond lengths of 0.963/0.962 Å, resulting in two ν_{OH}^{s} and two ν_{OH}^{a} modes at 3654/6 and 3743/5 cm^{-1}, respectively. ICPT further contracts the C–C bonds parallel to the C_3 axis (initially stretched by the Jahn–Teller distortion) by up to 12 mÅ to 1.568/9 Å compared to $[Ad(H_2O)_2(I)]^+$, and they increasingly approach the bond lengths of neutral Ad (r_{CC} = 1.538 Å) and Ady (r_{CC} = 1.560 Å). The C–C bonds at the top of Ad^+ are slightly shortened (by up to 3 mÅ) and the C–C bonds at the bottom of Ad^+ are slightly elongated (by up to 5 mÅ). Moreover, the C–H bonds at the top of Ad^+ are slightly elongated (by up to 2 mÅ), while the remaining C–H bonds are hardly affected by ICPT ($\Delta r_{CH} < 1$ mÅ).

In the $n = 3$ isomers II–IV (E_0 = 10.8, 11.2, 12.0 kJ mol^{-1}), the additional H_2O is attached to the terminal H_2O of $[Ad(H_2O)_2(I)]^+$ and they differ only in the orientation of the formed $(H_2O)_3$ chain bound to Ad^+. Nevertheless, ICPT occurs in all three isomers and the H_3O^+ core ion is twofold solvated by Ady and a $(H_2O)_2$ dimer. Unlike in isomer I, $\nu_{OH\cdots C}$ and ν_{OH}^{b} of H_3O^+ are coupled in II–IV, resulting in an antisymmetric, $(\nu_{OH}^{b}/\nu_{OH\cdots C})^{a}$ = 1735, 1697, and 1683 cm^{-1}, and a symmetric normal mode, $(\nu_{OH}^{b}/\nu_{OH\cdots C})^{s}$ = 2021, 1982, and 2075 cm^{-1}, for each isomer. The O···HO H-bonds in the $(H_2O)_2$ unit are weaker, leading to ν_{OH}^{b} at 3205, 3142, and 3222 cm^{-1} for II–IV, respectively.

Isomer V (E_0 = 15.5 kJ mol^{-1}) is formed by adding H_2O to $[Ad(H_2O)_2(III)]^+$ so that a $(H_2O)_3$ trimer binds with the central H_2O molecule to a CH_2 group of Ad^+. This in turn causes ICPT leading to a fully solvated H_3O^+ core ion with one Ady and two H_2O ligands. In contrast to isomer I with a 1-Ady ligand, isomer V has a 2-Ady ligand, which is a less stable configuration with an almost linear OH···C H-bond (1.734 Å, 175.4°) and $D_0(H_7O_3^+)$ = 78.5 kJ mol^{-1}. The O–H bond of H_3O^+ is much shorter than in isomer I (r_{OH} = 1.037 *vs.* 1.068 Å), resulting in a less redshifted intensive ν_{OH}^{b} mode at 2366 cm^{-1}. The OH···O H-bonds are substantially stronger, shorter, and more linear than in I ($r_{OH\cdots O}$ = 1.550/5 *vs.* 1.578 Å, ϕ_{OHO} = 173.9°/176.1° *vs.* 172.1°/172.7°, $E^{(2)}$ = 79.7/78.8 *vs.* 70.0/68.8 kJ mol^{-1}) leading to larger redshifts of the corresponding coupled ν_{OH}^{b} modes down to 2744 and 2838 cm^{-1}.

The IRPD spectrum of $[Ad(H_2O)_3]^+$ is compared in Fig. 7 to the IR spectra calculated for isomers I–V and the vibrational assignments are listed in Table S3 (ESI†). The IR spectrum

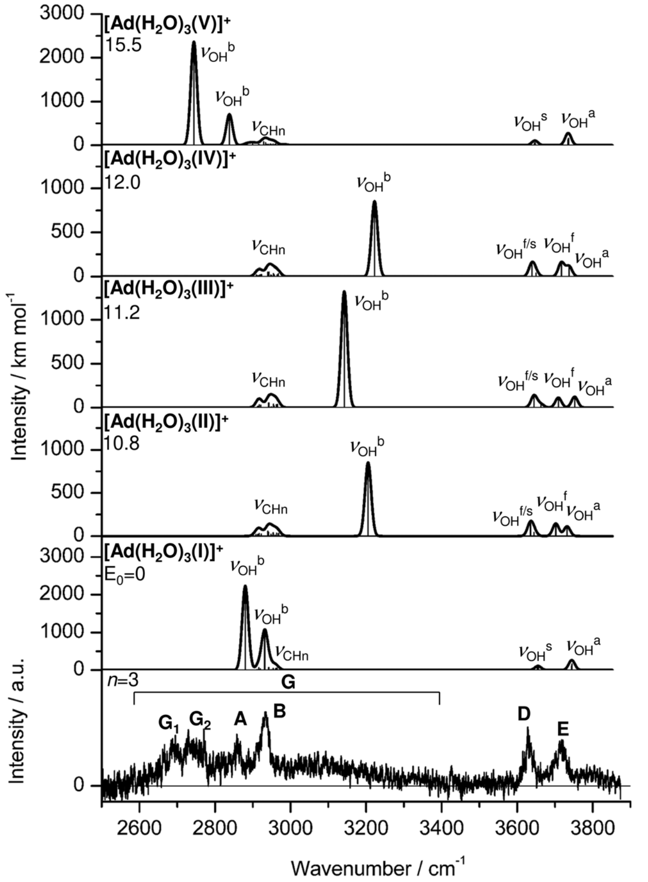

Fig. 7 IRPD spectrum of $[Ad(H_2O)_3]^+$ compared to linear IR absorption spectra of $[Ad(H_2O)_3(I–V)]^+$ calculated at the B3LYP-D3/cc-pVTZ level. Note the different IR intensity scales for the computed IR spectra. The positions of the transition observed in the IRPD spectrum of $[Ad(H_2O)_3]^+$ and their vibrational assignment are listed in Table S3 (ESI†). Differences in relative energy (E_0) are given in kJ mol^{-1}.

computed for the global minimum $[Ad(H_2O)_3(I)]^+$ agrees well with the observed bands A, B, D, and E, and also explains the absence of band F in the $n = 3$ spectrum, since no ν_{OH}^{f} mode exists for this isomer. The most intense ν_{CH_n} modes of isomer I at 2916 and 2942 cm^{-1} can be assigned to bands A (2858 cm^{-1}) and B (2934 cm^{-1}). The free OH stretch modes ν_{OH}^{s} (3654/6 cm^{-1}) and ν_{OH}^{a} (3743/5 cm^{-1}) fit to bands D (3628 cm^{-1}) and E (3718 cm^{-1}). The rather intense ν_{OH}^{b} modes predicted at 2880 and 2931 cm^{-1} are attributed to the rather broad bands G_1 and G_2, with deviations of 185 and 180 cm^{-1}, respectively. These somewhat larger deviations are ascribed to the greater anharmonicity of these proton donor stretch modes, which are not well compensated for by scaled harmonic frequencies. Indeed, the spacing between G_1 and G_2 and between the assigned ν_{OH}^{b} modes are quite similar (56 *vs.* 51 cm^{-1}), strongly supporting the suggested assignment. While isomer I is capable to fully explain all bands observed in the measured IRPD spectrum and thus our favoured assignment, some minor populations of the higher-energy isomers with $E_0 >$ 10 kJ mol^{-1} cannot fully be excluded. For example, the characteristic intense ν_{OH}^{b} modes of isomers II–IV in the spectral range 3100–3000 cm^{-1} may contribute to some extent to the broad background G. However, the associated ν_{OH}^{f} modes are not clearly resolved as band F in the IRPD spectrum (unlike, for example, in the $n = 4$ spectrum), indicating that their population is at most minor. At first glance, the IR spectrum of V agrees well with the IRPD spectrum, being quite similar to that isomer I. However, the computations typically strongly underestimate the redshift of the proton donor stretch modes, making the apparent agreement of the predicted ν_{OH}^{b} modes with bands G_1 and G_2 artificial. Moreover, unlike for isomer I, the spacing between the two ν_{OH}^{b} modes is substantially larger than the gap between the experimental bands (94 *vs.* 56 cm^{-1}). In conclusion, our analysis suggests that isomer I is by far the predominant carrier of the measured IRPD spectrum.

4.5. $[Ad(H_2O)_4]^+$

20 low-energy isomers are computed for $[Ad(H_2O)_4]^+$ (Fig. 8 and Fig. S15, S16, Table S8, ESI†). An important aspect of the larger and more flexible clusters with $n \geq 4$ is that entropic effects play a more crucial role in their relative energies than for the more rigid smaller clusters with $n \leq 3$. To this end, we also discuss free energies (at room temperature) that favour isomers with flexible hydration structures (*e.g.*, single ligands) over rigid structures (*e.g.*, cyclic rings or longer solvent chains interacting with the Ady cage). For example, while the energetic order for the four $[Ad(H_2O)_4]^+$ isomers in Fig. 8 is I–IV, with E_0 = 0, 0.2, 4.9, and 11.0 kJ mol^{-1}, their free energies vary as G_0 = 0, −6.5, −0.2, and 7.5 kJ mol^{-1}, meaning that II becomes more stable than I at elevated temperature. This temperature effect can become an issue because cooling in the supersonic plasma expansion may be incomplete (the effective temperature is difficult to estimate) and kinetic trapping can occur. In the following, only isomers I–IV are discussed, because their free energy differences are less than 15 kJ mol^{-1}. Their structures are shown in Fig. 8 and Fig. S11 (ESI†), and their computed IR spectra are compared with the IRPD spectrum in Fig. 9.

Isomer I of $n = 4$ ($E_0 = 0$, $G_0 = 0$) with C_s symmetry is formed from $[Ad(H_2O)_3(I)]^+$ by adding H_2O to the terminal H_2O ligands, resulting in a cyclic $H^+(H_2O)_4$ structure, in which Ady is attached to the H_3O^+ ion. The hydration network has two equivalent stronger OH···O ionic H-bonds (1.556 Å, 167.9°, $E^{(2)}$ = 80.8 kJ mol^{-1}) of two H_2O ligands (single-donor single-acceptor) to H_3O^+ and two equivalent and significantly weaker neutral OH···O H-bonds (1.927 Å, 158.4°, $E^{(2)}$ = 16.9 kJ mol^{-1}) to the terminal H_2O (double acceptor) closing the hydration ring. Due to formation of the cyclic ring, the proton-donor O–H bonds are elongated by 9/10 mÅ to 1.018/0.973 Å compared to $[Ad(H_2O)_3(I)]^+$. The H_3O^+ ion of the ring is connected *via* a strong OH···C ionic H-bond (1.666 Å, 173.9°, $E^{(2)}$ = 36.7 kJ mol^{-1}) to the tertiary C radical center of Ady. This OH···C bond is longer, weaker, and less linear than for $[Ad(H_2O)_3(I)]^+$ (1.626 Å, 180.0°, $E^{(2)}$ = 43.7 kJ mol^{-1}). As a result, the O–H donor bond contracts by 14 mÅ to 1.054 Å. Because ICPT has already occurred at $n = 3$, the charge transfer increases only slightly by 20 m*e* to 895 m*e* and the influence of the fourth H_2O molecule on the structure of the Ady cage is negligible

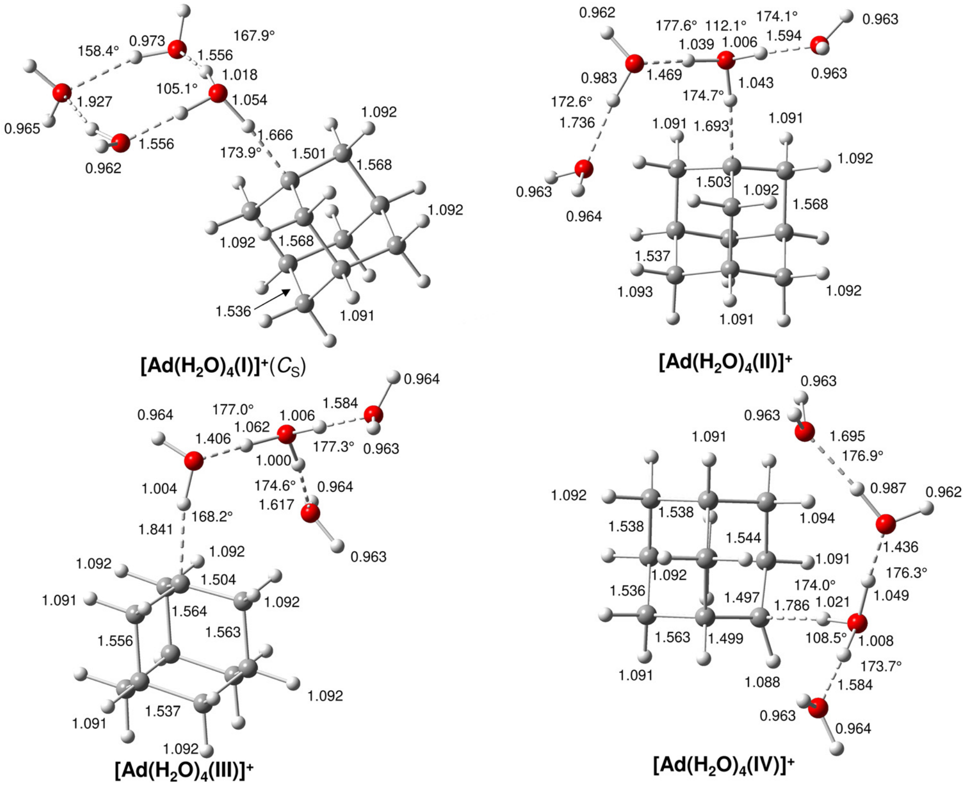

$[Ad(H_2O)_4(I)]^+(C_S)$ **$[Ad(H_2O)_4(II)]^+$** **$[Ad(H_2O)_4(III)]^+$** **$[Ad(H_2O)_4(IV)]^+$**

Fig. 8 Calculated equilibrium structures (in Å and degrees) of $[Ad(H_2O)_4(I–IV)]^+$ in their ground electronic state (B3LYP-D3/cc-pVTZ). All bond lengths are shown in Fig. S11 (ESI†).

($\Delta r_{CC} < 1$ mÅ, $\Delta r_{CH} < 1$ mÅ). The IR spectrum predicted for $[Ad(H_2O)_4(I)]^+$ is characterized by two intense and moderately redshifted $\nu_{OH}^{b\text{-ring}}$ modes at 3484/3509 cm^{-1}, three intense and strongly redshifted ν_{OH}^{b} modes of the H_3O^+ ion at 2118/2688/2829 cm^{-1}, and two weaker and almost unshifted $\nu_{OH}^{f\text{-ring}}$ modes at 3711/3714 cm^{-1}, as well as ν_{OH}^{a} and ν_{OH}^{s} modes of the terminal H_2O at 3631/3713 cm^{-1}.

The second most stable isomer II on the potential energy surface (E_0/G_0 = 0.2/−6.5 kJ mol^{-1}) becomes the global minimum on the free energy surface due to the higher flexibility of its chain-like $H^+(H_2O)_4$ unit compared to the rigid cyclic ring of isomer I. Isomer II can also be formed by adding H_2O to $[Ad(H_2O)_3(I)]^+$ but in this case the additional ligand binds to one of the terminal H_2O molecules. The resulting chain has one strong OH···O H-bond (1.469 Å, 177.6°, $E^{(2)}$ = 117.4 kJ mol^{-1}), one slightly weaker OH···O H-bond (1.594 Å, 174.1°, $E^{(2)}$ = 66.5 kJ mol^{-1}), and one weak OH···O H-bond (1.736 Å, 172.6°, $E^{(2)}$ = 35.7 kJ mol^{-1}). The $H^+(H_2O)_4$ chain binds again *via* H_3O^+ to the Ady radical by an even weaker OH···C H-bond (1.693 Å, 174.7°, $E^{(2)}$ = 31.6 kJ mol^{-1}). As a result, the proton donor O–H bond of H_3O^+ contracts more (1.043 Å). The charge transfer increases only slightly by 31 m*e* to 906 m*e* (Fig. S6, ESI†), again resulting in only minor changes in the Ady cage ($\Delta r_{CC} < 2$ mÅ, $\Delta r_{CH} < 2$ mÅ). The IR spectrum of $[Ad(H_2O)_4(II)]^+$ is characterized by three intense and strongly redshifted ν_{OH}^{b} modes of H_3O^+ (2223/2447/2940 cm^{-1}), one less intense and moderately redshifted ν_{OH}^{b} mode at 3305 cm^{-1}, one weaker and almost unshifted ν_{OH}^{f} mode at 3708 cm^{-1}, and two ν_{OH}^{a} and ν_{OH}^{s} modes of the terminal H_2O molecules at 3648/3651 and 3736/3740 cm^{-1}, respectively.

Isomer III (E_0/G_0 = 4.9/0.2 kJ mol^{-1}) is formed by adding H_2O to the central ligand of $[Ad(H_2O)_3(IV)]^+$, causing the excess proton to migrate by one unit, leading to a true Eigen-type $H^+(H_2O)_4$ structure with Ady binding in the second shell of H_3O^+. Ady breaks the symmetry of the Eigen ion and, due to cooperativity, the OH···O ionic H-bond of H_3O^+ to H_2O with Ady is strongest (1.406 Å, 177.0°, $E^{(2)}$ = 153.0 kJ mol^{-1}), while the other two are somewhat weaker (1.584/1.617 Å, 177.3°/174.6°, $E^{(2)}$ = 69.9/60.3 kJ mol^{-1}). The Eigen ion is bound to Ady *via* a weak OH···C H-bond (1.841 Å, 168.2°, $E^{(2)}$ = 16.2 kJ mol^{-1}) and the proton donor O–H bond contracts by 85 mÅ to 1.004 Å. As a result, the IR spectrum predicted for III exhibits intense redshifted ν_{OH}^{b} modes at 2055, 2915, and 3034 cm^{-1} and $\nu_{OH\cdots C}$ at 2883 cm^{-1}. Due to ICPT, nearly all positive charge is again located on $H^+(H_2O)_4$ (q = 948 m*e*) (Fig. S6, ESI†).

In isomer IV (E_0/G_0 = 11.0/7.5 kJ mol^{-1}), a $H^+(H_2O)_4$ chain is attached to a former CH_2 group *via* an OH···C H-bond of Ady to the H_3O^+ ion. It may be formed by adding H_2O to $[Ad(H_2O)_3(V)]^+$. The three OH···O bonds of the solvent chain are strong (1.436 Å, 176.3°, $E^{(2)}$ = 132.1 kJ mol^{-1}), slightly weaker (1.584 Å, 173.7°, $E^{(2)}$ = 69.2 kJ mol^{-1}), and weak (1.695 Å, 176.9°, $E^{(2)}$ = 41.5 kJ mol^{-1}), resulting in ν_{OH}^{b} modes at 2228, 2915, and 3248 cm^{-1}, repectively. Addition of H_2O

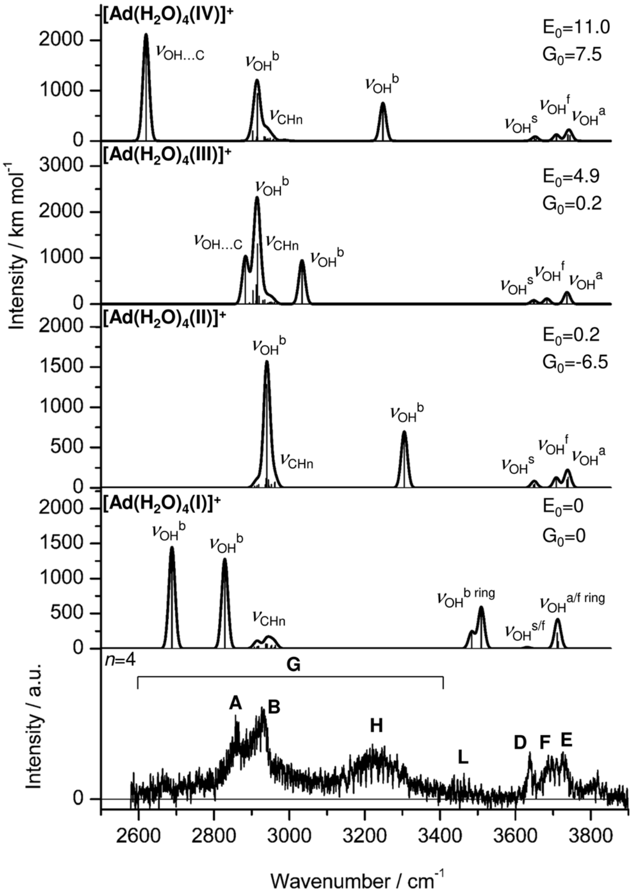

Fig. 9 IRPD spectrum of $[\mathrm{Ad(H_2O)_4}]^+$ compared to linear IR absorption spectra of $[\mathrm{Ad(H_2O)_4(I–IV)}]^+$ calculated at the B3LYP-D3/cc-pVTZ level. Note the different IR intensity scales for the computed IR spectra. The positions of the transition observed in the IRPD spectrum of $[\mathrm{Ad(H_2O)_4}]^+$ and their vibrational assignment are listed in Table S4 (ESI†). Differences in relative energy (E_0) are given in kJ mol^{-1}.

weakens the OH···C H-bond to Ady (1.786 *vs.* 1.734 Å, 174.0° *vs.* 175.4°, $E^{(2)} = 16.7$ *vs.* 21.8 kJ mol^{-1}) and the O–H proton donor bond is shorter than in $[\mathrm{Ad(H_2O)_3(V)}]^+$ (1.021 *vs.* 1.037 Å), resulting in a less redshifted $\nu_{\mathrm{OH}}^{\mathrm{b}}$ mode at 2620 cm^{-1}. The charge on $\mathrm{H^+(H_2O)_4}$ is increased to 915 m*e* (Fig. S6, ESI†).

The IR spectra calculated for I–IV are compared to the experimental IRPD spectrum of $n = 4$ in Fig. 9 and the vibrational assignments are listed in Table S4 (ESI†). The IRPD bands A, B, D, and E assigned to free ν_{CH_n} and $\nu_{\mathrm{OH}}^{\mathrm{s/a}}$ modes are less structure-sensitive and compatible with all four computed isomers. The more isomer-selective bands are H, L, and F. The presence of I with a cyclic solvent ring is uniquely indicated by the weak band L ($\nu_{\mathrm{OH}}^{\mathrm{b\text{-}ring}}$ at 3484/3509 cm^{-1}). Isomer I can also explain the high relative intensity of band F at 3692 cm^{-1}. Its intense $\nu_{\mathrm{OH}}^{\mathrm{b}}$ modes predicted at 2688 and 2829 cm^{-1} are not observed in the considered spectral range, probably because the calculations underestimate their redshifts. Significantly, isomer I cannot account for band H at 3220 cm^{-1} and the triple feature of the free OH stretch bands (D–F). On the other hand, isomer II, which is most stable on the free energy surface, can readily explain H by its $\nu_{\mathrm{OH}}^{\mathrm{b}}$ mode at 3305 cm^{-1} and all other bands (apart from L), with summed, mean, and maximum deviations of 31, 21, and 85 cm^{-1} (without G). Its intense $\nu_{\mathrm{OH}}^{\mathrm{b}}$ mode at 2940 cm^{-1} is assigned to the broad background G and may be responsible for the increased signal between bands A and B when compared to the IRPD spectra of the other cluster sizes. While all experimental bands can fully be explained by isomers I and II, the minor presence of the higher-energy isomers III and IV cannot be ruled out. Assuming that only isomers I and II are detected, their population ratio may roughly be estimated as 1 : 10 from the ratio of the integrated intensities of bands H and L and the corresponding computed IR oscillator strengths.

4.6. $[\mathrm{Ad(H_2O)_5}]^+$

20 low-energy isomers are calculated for $[\mathrm{Ad(H_2O)_5}]^+$ (Fig. S17–S19 and Table S9, ESI†). However, the number of possible isomers is probably even higher due to the flexible $\mathrm{H^+(H_2O)_5}$ structures. The most stable isomers I–XIII with $E_0 <$ 18 kJ mol^{-1} have exclusively structures with an $\mathrm{H^+(H_2O)_5}$ core ion to which Ady is attached at the surface. There is a large energy gap of >20 kJ mol^{-1} between isomer XIII and XIV–XX ($E_0 >$ 38 kJ mol^{-1}), in which individual $\mathrm{H_2O}$ molecules are separately attached to the Ady cage *via* weak dipole forces. For these energetic reasons and from the analysis of the IRPD spectra for $n \leq 4$, we conclude that only isomers with a $\mathrm{H^+(H_2O)_5}$ core ion solvated by Ady cage are produced in the ion beam. The assignment of the IRPD bands is analogous to that of the $n = 1–4$ spectra, *i.e.*, bands A and B are assigned to ν_{CH_n} modes and bands D, F, and E to $\nu_{\mathrm{OH}}^{\mathrm{a/s/f}}$ modes. Band L can probably be attributed to $\nu_{\mathrm{OH}}^{\mathrm{b\text{-}ring}}$ modes, which are redshifted compared to that of $n = 4$. The broad signal G can again be assigned to $\nu_{\mathrm{OH}}^{\mathrm{b}}$ modes of strong ionic OH···O H-bonds and band H to $\nu_{\mathrm{OH}}^{\mathrm{b}}$ modes of weaker OH···O H-bonds. Due to the large number of possible low-energy structures with partly similar computed IR spectra, isomer-specific assignments are hardly possible without isomer-specific spectroscopy and therefore the $[\mathrm{Ad(H_2O)_5}]^+$ spectrum will not be discussed in detail further.

5. IRPD spectra in the fingerprint range

Analysis of the IRPD spectra of $[\mathrm{Ad(H_2O)}_{n=1-5}]^+$ in the CH/OH stretch range using B3LYP-D3 calculations provides a clear indication for ICPT between $n = 2$ and 3, which shall be confirmed by observation of the relevant and strongly redshifted CH···O and/or OH···C proton donor stretch modes predicted in the fingerprint range. As shown in Fig. 10, the $\nu_{\mathrm{CH\cdots O}}$ mode of $[\mathrm{Ad(H_2O)(I)}]^+$ is predicted at 2033 cm^{-1} due to the strong ionic CH···O H-bond. For $[\mathrm{Ad(H_2O)_2(I)}]^+$, this $\nu_{\mathrm{C\cdots H\cdots O}}$ mode shifts even further down to 818 cm^{-1}, because the proton is roughly equally shared between Ady and $\mathrm{(H_2O)_2}$. For $[\mathrm{Ad(H_2O)_3(I)}]^+$, ICPT is complete and the proton donor stretch mode of the strong OH···C ionic H-bond shifts back to the blue and is predicted at 1953 cm^{-1}. To confirm this trend

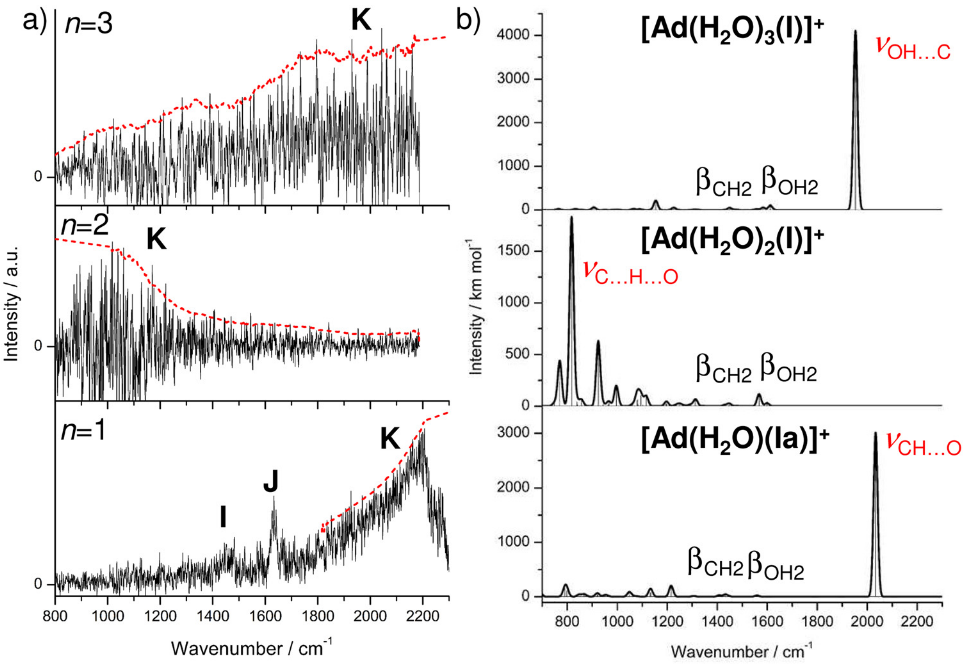

Fig. 10 (a) IRPD spectra of $[Ad(H_2O)_{n=1-3}]^+$ in the fingerprint range (800–2200 cm^{-1}). Red dotted lines are added to illustrate the signal rise of bands K and to indicate possible out-of-range signals. The positions of transitions I and J as well as the roughly estimated positions of bands K and their vibrational assignments are listed in Table 1. (b) Calculated IR spectra of $[Ad(H_2O)(Ia)]^+$, $[Ad(H_2O)_2(I)]^+$, and $[Ad(H_2O)_3(I)]^+$ in the fingerprint range. The significant proton stretch modes are marked in red color.

signaling the ICPT between n = 1 and 3 experimentally, IRPD spectra of $[Ad(H_2O)_{n=1-3}]^+$ are measured in the fingerprint range (800–2200 cm^{-1}, Fig. 10). However, due to the lower photon energies ($E_{h\nu}$ = 9–26 kJ mol^{-1}) and photon flux of the IR laser in this frequency range compared to the high H_2O binding energies ($D_0(H_2O)$ = 46, 61, 67 kJ mol^{-1} for isomer I of n = 1–3), only broad and unresolved IRPD spectra with low signal-to-noise ratios are obtained under the employed single-photon absorption conditions. This is particularly true for the broad proton donor stretch bands (as already observed in the CH/OH stretch range). To reduce the effective internal temperature and dissociation energy of the clusters (and thus to improve the signal-to-noise ratio of the fingerprint spectra), we tried to produce weakly-bonded $[Ad(H_2O)_n]^+$-Ar clusters which have low Ar binding energies (D_0(Ar) < 10 kJ mol^{-1}).[37,39,68,74] However, the achieved yield of such Ar-tagged clusters has been too low for IRPD experiments, probably due to efficient Ar → H_2O ligand exchange during cluster generation in the supersonic plasma expansion. Nevertheless, salient qualitative information about the ICPT can be extracted from the IRPD spectra of the untagged clusters in Fig. 10.

The IRPD spectrum of n = 1 exhibits the best signal-to-noise ratio because its H_2O binding energy is lowest and the observed bands occur in the higher frequency fingerprint range, *i.e.* at higher photon energies. Two narrower transitions I and J are observed at 1461 and 1633 cm^{-1} and assigned to convoluted transitions of the β_{CH_2} and β_{OH_2} modes of $[Ad(H_2O)(Ia/Ib)]^+$ predicted at 1433/2 and 1558/9 cm^{-1} (Fig. S23 and Table S1, ESI†), respectively. Although these bands could also be assigned to the β_{CH_2} and β_{OH_2} modes of isomers II and III, these are excluded from the analysis of the IRPD spectrum in the CH/OH stretch range. In addition, a broad and intense transition K is observed, whose signal rises at ∼1800 cm^{-1} and increases until the IR laser intensity approaches zero (>2200 cm^{-1}). Unfortunately, approaching this spectral range from the high frequency side suffers from the same problem, preventing a determination of the peak maximum which can only be estimated as $2200 \leq \nu_K \leq 2600$ cm^{-1}. However, band K can clearly be identified as the $\nu_{CH\cdots O}$ mode of $[Ad(H_2O)(Ia/Ib)]^+$ predicted at 2030 cm^{-1} due to its large width, which is typical for proton donor stretch transitions,[66–71] and its frequency range, which cannot contain other intense transitions.

The signal-to-noise ratio of the n = 2 spectrum is smaller than for the n = 1 spectrum and does not allow a reliable determination of band maxima. However, two important qualitative observations can be made. First, the broad and intense signal in the higher frequency range observed for n = 1 (1800–2200 cm^{-1}) has disappeared. Second, despite the low photon energy, a new strong signal K (≲1000 cm^{-1}) not present in the n = 1 spectrum appears in the lower frequency range (900–1200 cm^{-1}) until the laser pulse energy approaches zero. Both observations confirm the predicted elongation of the acidic C–H bond of Ad^+ upon addition of the second H_2O ligand and the resulting redshift of the $\nu_{C\cdots H\cdots O}$ mode of $[Ad(H_2O)_2(I)]^+$ predicted at 818 cm^{-1}. The n = 3 spectrum shows again a different picture, with almost no signal detected in the lower frequency range (900–1200 cm^{-1}) and increasing signal toward the higher frequency range starting from ∼1500 cm^{-1}

and then remaining constant from 1700 to 2200 cm^{-1}, indicating a transition K with $\nu_K \geq 1700$ cm^{-1}. This observation supports the predicted blueshift of the $\nu_{OH\cdots C}$ mode to 1953 cm^{-1} of $[Ad(H_2O)_3(I)]^+$ after completed ICPT to the $(H_2O)_3$ cluster. In conclusion, although the quality of the IRPD spectra in the fingerprint is limited, they fully reproduce the predicted band shifts caused by ICPT occurring in the size range n = 1–3.

6. Further discussion

Analysis of the IRPD spectra of $[Ad(H_2O)_n]^+$ in the CH/OH stretch (n = 1–5) and fingerprint ranges (n = 1–3) by B3LYP-D3 calculations provides a consistent picture of the sequential cluster growth and reactivity of this fundamental diamondoid radical cation, with clear evidence for hydration-induced ICPT for $n \geq 3$. All main bands of the IRPD spectra of $[Ad(H_2O)_{n\leq 4}]^+$ in the CH/OH stretch range can be assigned to the energetically most stable isomers (I). For n = 4, the free energies must be taken into account, which change the energetic order so that the isomer II becomes more stable at room temperature than isomer I.

In the n = 1 monohydrate, the H_2O ligand activates the acidic C–H bond of Ad^+ by forming a strong CH···O ionic H-bond stabilized mostly by cation-dipole forces. Because the calculated PA of Ady is substantially higher than that of H_2O (868 *vs.* 691 kJ mol^{-1})[60] and the ionization energy of Ad is much lower than that of H_2O (9.25 *vs.* 12.6 eV),[60] there is no proton transfer and only a minor charge transfer from Ad^+ to the ligand (Δq = 124 me). The second H_2O ligand prefers binding to the first H_2O ligand *via* an OH···O H-bond by more than 20 kJ mol^{-1} to further interior ion solvation of the Ad^+ cation by individual ligands. Apparently, strong cooperative effects arising from polarization forces of the nearby positive charge strongly stabilize the H-bonded solvent network and lead to the onset of ICPT to the solvent. Starting from n = 3, ICPT from Ad^+ to the $(H_2O)_n$ cluster is complete and the microhydration network expands as a H-bonded $H^+(H_2O)_n$ network to which the Ady radical is attached at the surface *via* a weak OH···C H-bond. For $n \geq 4$, the OH···C H-bond becomes even weaker due to the increasing PA of the H-bonded solvent network. The latter becomes more flexible giving rise to more competing low-energy $H^+(H_2O)_n$ isomers attached to the Ady cage. Thus, for n = 4 entropy becomes important and minor populations of energetically less stable isomers can be identified. Overall, due to the acidic C–H bond of Ad^+ and the hydration-induced ICPT to solvent, which transfers the positive charge to the water cluster, isomers with a H-bonded solvent network are preferred to isomers in which individual H_2O ligands solvate Ad^+ or Ady *via* (induced) dipole forces supported by weak CH···O contacts. The calculated terminal hydration energies for the identified $[Ad(H_2O)_n]^+$ clusters increase until ICPT is complete (D_0 = 46, 61, 69 kJ mol^{-1} for n = 1–3) and the H_3O^+ ion is fully solvated in an Eigen-type structure. For n = 4, the hydration energy decreases again (D_0 = 58 kJ mol^{-1}), because the added H_2O ligand is not directly bonded to H_3O^+ but located in the second hydration shell leading to an OH···O H-bond with much less ionic character.

The hydration energies (46–69 kJ mol^{-1} for n = 1–4) exceed by far the energy of the absorbed IR photon ($h\nu \ll 48$ kJ mol^{-1} 4000 cm^{-1}), indicating that only cluster ions with significant internal energy can undergo the IRPD process under the employed conditions of single-photon absorption. This aspect explains the widths of the transitions and the entropy contributions required to evaluate the energetic ordering of the isomers for $n \geq 4$. Furthermore, it accounts for the limited signal to noise ratio of the fingerprint spectra, because the IR photon energy is even lower ($10 < h\nu < 26$ kJ mol^{-1}), which further reduces the population of clusters with sufficient internal energy for the IRPD process. Nonetheless, the fingerprint spectra are of sufficient quality to fully confirm the size-dependence of ICPT. In addition to the IRPD spectra, ICPT at n_c = 3 is consistent with CID spectra of $[Ad(H_2O)_3]^+$ *via* observation of $H_7O_3^+$ (Fig. S2, ESI†) and the comparison of the PA of Ady (calculated as 868 kJ mol^{-1}) with the increasing PA values of $(H_2O)_n$ clusters (PA = 691, 808, 862, 900, 904, and 908 kJ mol^{-1} for n = 1–6),[53–57] which predict ICPT for $n \geq 3$ (Fig. 11). The size-dependent ICPT is also visible in the electron spin densities. These increase for the most stable isomers of n = 1–4 as $s = 0.195 < 0.381 < 0.640 < 0.681$ on the apical C atom, which develops gradually into a tertiary radical center between n = 1 and 3, when Ada^+ transforms to Ady upon ICPT. Overall, the spin density remains mostly on the diamondoid moiety for all cluster sizes, with s = 0.800, 0.747, 0.863, and 0.886 on Ady for n = 1–4. In this sense, the radical character remains always on the open-shell Ada^+ or Ady part, while the closed-shell $(H_2O)_n$ or $H^+(H_2O)_n$ solvent cluster carries only low spin density. As a result, in the $n \geq 3$ clusters, the spin and radical center localized on the diamondoid radical is separated

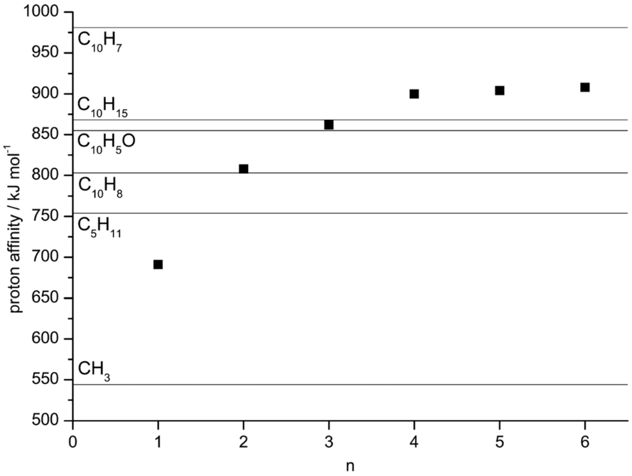

Fig. 11 Proton affinities of $(H_2O)_n$ clusters as a function of the cluster size n (PA = 691, 808, 862, 900, 904, 908 kJ mol^{-1} for n = 1–6),[53–57] compared with the proton affinities of various X radicals: PA = 544, 754, 803, 855, 868, and 981 kJ mol^{-1} for X = CH_3 (methyl, n_c = 1), C_5H_{11} (pentyl, n_c = 2),[78] $C_{10}H_8$ (naphthalene, n_c = 2),[68] C_6H_5O (phenoxyl, n_c = 3),[86] $C_{10}H_{15}$ (Ady, n_c = 3), and $C_{10}H_7$ (naphthyl, $n_c \gg 5$).[35]

from the positive charge localized on the solvent cluster (distonic cluster ion).

The detailed evolution of the properties ($\nu^{\rm calc}_{\rm CH/OH}$, $\nu^{\rm exp}_{\rm CH/OH}$, $r_{\rm CH/OH}$, $E^{(2)}$) of the acidic C–H bond of Ad^+ and the O–H bonds of the solvent cluster of the most stable $\{Ad(H_2O)_{n=0-4}(I)\}^+$ clusters as a function of n is shown in Fig. 12. The following colour code is used to distinguish between the different vibrations and their corresponding bonds and energies: $\nu^{\rm a}_{\rm OH}$ (orange), $\nu^{\rm s}_{\rm OH}$ (green), $\nu^{\rm f}_{\rm OH}$ (magenta), $\nu^{\rm b}_{\rm OH}$ (blue), $\nu_{\rm OH\cdots C}$ (violet), $\nu_{\rm CH\cdots O}$ (red). In general, the pattern of calculated and measured $\nu_{\rm OH/CH}$ frequencies agree well in terms of incremental changes, although the absolute values sometimes differ, mainly due to improper evaluation of the anharmonicity of these modes, especially for the proton donor stretch vibrations. The $\nu_{\rm OH}$ modes show the typical behavior of a growing water solvent network. While $\nu^{\rm a/s}_{\rm OH}$ (green, orange) have almost the same frequencies with a minor blueshift (bands E and D) with increasing n and also $\nu^{\rm f}_{\rm OH}$ (magenta) have a negligible redshift (bands F), the $\nu^{\rm b}_{\rm OH}$ modes (blue) are strongly redshifted due to the formation of strong OH···O H-bonds. However, for n = 2 and 3, H_2O ligands bind to a H_3O^+ ion which is in the process of being formed by ICPT, resulting in stronger ionic H-bonds and thus even larger redshifts of $\nu^{\rm b}_{\rm OH}$ (bands $G_{(1/2)}$) than, for example, in the hydration network of the amantadine$^+$ radical cation which does not exhibit hydration-induced ICPT.[29] This trend for n = 2 and 3 also fits the calculated larger O–H bond lengths ($r_{\rm OH}$ = 1.003 and 1.008 Å) and $E^{(2)}$ energies (58.9 and 70.0/68.8 kJ mol^{-1}). Further water addition (n = 4) leads again to a weaker OH···O H-bond ($r_{\rm OH}$ = 0.983 Å, $E^{(2)}$ = 35.7 kJ mol^{-1}), resulting in a new and less redshifted $\nu^{\rm b}_{\rm OH}$ mode (band H). However, due to the enhanced cooperative effect of the protonated water network, one $\nu^{\rm b}_{\rm OH}$ mode is shifted even further into the red and outside the observed spectral range (<2600 cm^{-1}), which agrees with stretching of the corresponding O–H donor bond to $r_{\rm OH}$ = 1.039 Å and the higher $E^{(2)}$ energy (117.4 kJ mol^{-1}).

Although the experimental $\nu_{\rm CH\cdots O/OH\cdots C}$ frequencies (red, violet) can only roughly be estimated by IRPD (indicated by error bars in Fig. 12), their evolution with increasing n agrees well with the predicted trend. The $\nu^{\rm t}_{\rm CH}$ mode, already redshifted by Jahn–Teller distortion upon ionization (n = 0), is further redshifted due to enhanced activation by the first H_2O ligand (n = 1), which agrees well with the observed band K. Because the NBO calculations consider the proton as a single fragment, it is not possible to obtain an $E^{(2)}$ energy of the CH···O H-bond for n = 1. For n = 2, the proton has almost equal distances to C (red) and O (violet) due to further stretching of the C–H bond. The NBO analysis reveals a very high $E^{(2)}$ energy (221 kJ mol^{-1}) between the lone pair of C and the antibonding σ* orbital of the O–H donor bond, because it already attributes the proton to the

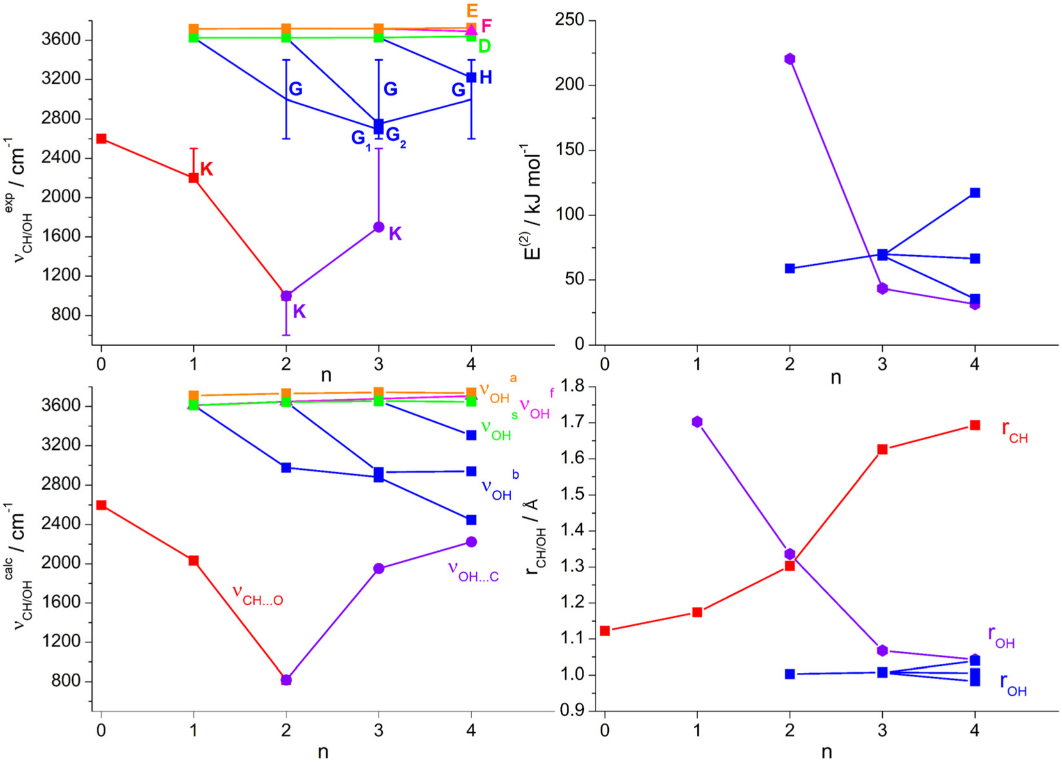

Fig. 12 Various calculated and experimental properties of the O–H bonds and the acidic C–H bond of the most stable $[Ad(H_2O)_{n=1-4}]^+$ clusters as a function of the cluster size n: calculated and experimental CH and OH stretch frequencies ($\nu_{\rm CH/OH}$); calculated C–H and O–H bond lengths ($r_{\rm CH/OH}$); calculated second-order perturbation energies ($E^{(2)}$) of donor–acceptor orbital interactions involved in the H-bonds. A colour code is used to distinguish between the different modes and their corresponding bonds and energies: $\nu^{\rm a}_{\rm OH}$ (orange); $\nu^{\rm s}_{\rm OH}$ (green); $\nu^{\rm f}_{\rm OH}$ (magenta); $\nu^{\rm b}_{\rm OH}$ (blue); $\nu_{\rm OH\cdots C}$ (violet), $\nu_{\rm CH\cdots O}$ (red). Experimentally observed peaks associated with $\nu_{\rm OH}$ modes and $\nu_{\rm CH}$ modes of the acid C–H bond are labeled (B, D, E, F, G, H, K). The rough experimentally determined frequencies of band K are indicated by error bars.

water cluster. The appearance of band K below 1000 cm^{-1} agrees well with the predicted redshifts of $\nu_{\mathrm{CH\cdots O}}$ (red) or $\nu_{\mathrm{OH\cdots C}}$ (violet). For n = 3, all data show that ICPT is complete. The distance of the proton to C (O) is dramatically increased (decreased) and the $E^{(2)}$ energy is significantly lower. This trend is consistent with a blueshift of $\nu_{\mathrm{OH\cdots C}}$ compared to n = 2 toward frequencies similar to that for n = 1, as experimentally confirmed by the increasing signal at 1700 cm^{-1} (K). At n = 4, this trend continues as the distance of the proton to C (O) increases (decreases) further and $E^{(2)}$ also decreases. The $\nu_{\mathrm{OH\cdots C}}$ mode shifts further to the blue and thus approaches the frequencies of the $\nu^{\mathrm{b}}_{\mathrm{OH}}$ modes.

Although the NBO analysis indicates complete ICPT to the solvent already at n = 2, the proton assignment to Ady or $(H_2O)_n$ is ambiguous for n = 2 because NBO analysis considers only localized orbitals and ignores delocalization effects. The CID spectrum of $[Ad(H_2O)_2]^+$ shows almost no $H_5O_2^+$ signal, while that of $[Ad(H_2O)_3]^+$ exhibits appreciable $H_7O_3^+$ signal which is roughly equal to the Ad$^+$ signal (Fig. S2, ESI†). These CID spectra thus argue against complete ICPT already at n = 2 as suggested by the NBO analysis. This view is also consistent with the calculated bond dissociation energies for the processes Ad$^+$ + $(H_2O)_n$ and Ady + $H^+(H_2O)_n$, which indicate ICPT between n = 2 and 3 (Fig. S24, ESI†). Therefore, we consider $[Ad(H_2O)_2(I)]^+$ to have a proton-shared structure, in which the proton is not completely transferred, and determine the critical cluster size for complete ICPT as n_c = 3, consistent with previous calculations.[27] Despite of the decreasing dissociation energy for the channel Ady + $H^+(H_2O)_n$ (D_0 = 221, 123, 93, 69 kJ mol^{-1} for n = 1–4), the dissociation energy for loss of a single H_2O ligand is always still lower (D_0 = 46, 61, 69, 58 kJ mol^{-1}) and thus the dominant IRPD channel for all considered n.

7. Comparison to related clusters

In the following, we compare the threshold for ICPT (n_c = 3) observed for the microhydrated Ad$^+$ cation (as a prototypical cycloalkane cation) with that of related linear alkane cations and aromatic hydrocarbons. A first rough indicator for the position of the proton in a $[X\cdots H\cdots(H_2O)_n]^+$ cluster is the difference in PA of X and $(H_2O)_n$. A second and in some cases even decisive factor is the difference between the solvation energies of $XH^+\cdots(H_2O)_n$ and $X\cdots H^+(H_2O)_n$.[70,75–77] From the linear alkane cations, we consider C_5H_{12} (pentane) and CH_4 as examples and have computed their microhydrated structures at the same computational level (B3LYP-D3, Fig. S25, ESI†). Ionization of CH_4 (T_d) produces the Jahn–Teller distorted cation (C_{2v}) and elongates the C–H bond from 1.088 to 1.121 Å (by 33 mÅ). This CH donor group is very acidic, and addition of a single H_2O ligand causes complete ICPT to produce CH_3–H_3O^+ (*i.e.*, n_c = 1) with a rather asymmetric proton bridge ($r_{\mathrm{OH/CH}}$ = 1.057/1.726 Å). This trend is consistent with the PA values of CH_3 and H_2O (544 and 691 kJ mol^{-1}). Longer alkane chains can better stabilize a positive charge. In the case of C_5H_{12}, ionization elongates the C–H bond from 1.094 to 1.125 Å (by 31 mÅ), and addition of a single H_2O ligand produces a proton-shared structure, while complete ICPT is observed at n_c = 2, as determined by previous IRPD experiments.[78] Hence, ICPT in $[C_5H_{12}(H_2O)_n]^+$ is rather similar to the one observed in $[Ad(H_2O)_n]^+$ apart from the smaller n_c value. Stretching of the C–H bond upon ionization is similar (Δr_{CH} = 31 *vs.* 30 mÅ), while further activation by monohydration is much stronger for $C_5H_{12}{}^+$ than for Ad$^+$ (Δr_{CH} = 224 *vs.* 51 mÅ), indicating higher CH acidity due to reduced delocalization of the charge in the smaller hydrocarbon molecule. Delocalization of the charge is even less pronounced in $CH_4{}^+$, leading to a more acidic C–H bond and smaller critical value for ICPT (n_c = 1). The geometric parameters of the shared proton bridges in $[C_5H_{12}(H_2O)]^+$ and $[Ad(H_2O)_2(I)]^+$ are comparable ($r_{\mathrm{OH/CH}}$ = 1.307/1.349 Å *vs.* 1.336/1.303 Å). Due to the slightly more stretched C–H bond, the predicted $\nu_{\mathrm{C\cdots H\cdots O}}$ frequency of $[C_5H_{12}(H_2O)]^+$ is even lower than that for $[Ad(H_2O)_2(I)]^+$ (660 *vs.* 818 cm^{-1}). While C–H bond activation by ionization has been reported for a variety of linear alkenes,[79] hydration-induced ICPT has only been investigated yet by spectroscopy for pentane$^+$.[78] In addition, mass spectrometry of bare alkane clusters observed ICPT (self protonation) upon ionization of the acidic CH proton to a neighboring alkane.[80,81]

When comparing Ad$^+$ with aromatic hydrocarbon ions, the benzene cation ($C_6H_6{}^+$) is less acidic and shows ICPT only at n_c = 4, as proven by IR and electronic spectroscopy.[31,56,82–85] The C–H bond acidity becomes significantly smaller when expanding $C_6H_6{}^+$ to polycyclic aromatic hydrocarbon cations. For example, in the case of microhydrated cationic naphthalene ($[C_{10}H_8(H_2O)_n]^+$), which has a size roughly comparable to that of Ad$^+$, no ICPT is observed up to n = 5.[35] For protonated naphthalene ($C_{10}H_9{}^+$), ICPT upon microhydration occurs at n_c = 2.[68] However, here $H^+(H_2O)_2$ is bound as a Zundel ion to naphthalene *via* strong OH$\cdots\pi$ ionic H-bonds, which is different from the OH$\cdots$C H-bonds in $[Ad(H_2O)_n]^+$. The acidity of the C–H bond of Ad$^+$ is close to that of the O–H bond in cationic phenol ($C_6H_5OH^+$),[86] which also requires at least three H_2O ligands to drive complete ICPT (n_c = 3). The determined critical cluster sizes n_c for hydration-inducted ICPT in the here considered $[XH\cdots(H_2O)_n]^+$ clusters are consistent with the PA values of the various X radicals and the $(H_2O)_n$ clusters (Fig. 11), indicating that differences in the solvation energies are not too different and thus not decisive in these cases.

8. Conclusions

The analysis of IRPD spectra of mass-selected $[Ad(H_2O)_n]^+$ clusters in the XH stretch (n = 1–5) and fingerprint ranges (n = 1–3) using DFT calculations provides the first spectroscopic information about this fundamental reaction intermediate in polar solution. It reveals detailed precise and molecular-level information about the acidity of the CH proton of Ad$^+$, the growth of the hydration network, and the hydration-induced ICPT to the $(H_2O)_n$ cluster at the critical threshold of n_c = 3. While all main bands observed in the IRPD spectra can readily be assigned to the energetically most stable structures for $n = 1–3$, several isomers probably contribute to the spectra of the larger clusters ($n = 4–5$). Although the isomer assignment is clear up to $n = 4$, the large number of possible low-energy isomers for $n = 5$ prevents a detailed isomer assignment, which requires isomer-specific laser spectroscopy in future work. Like for linear alkanes, ionization of Ad weakens the apical C–H bond, which is further activated by sequential microhydration. For $n = 1$, a strong ionic CH···O H-bond is formed in an $Ad^+···H_2O$ cation–dipole complex with nearly free internal H_2O rotation.[30] For $n > 1$, all further H_2O molecules bind to the initial H_2O ligand *via* OH···O H-bonds, forming a H-bonded hydration network stabilized by strong cooperative effects arising from polarisation forces of the excess charge. Such a cluster growth is clearly preferred to interior ion solvation, in which individual H_2O ligands solvate the Ad^+ cation. Due to the increasing PA of the $(H_2O)_n$ clusters, the acidic CH proton of Ad^+ is progressively shifted toward the solvent cluster. The $n = 2$ cluster is characterized by a shared C···H···O proton bond with nearly equal C–H and O–H bond lengths. For $n_c = 3$, the proton is completely transferred to the solvent, leading to the formation of a H_3O^+ ion fully solvated by two H_2O ligands and an Ady radical (similar to the Eigen ion of $H^+(H_2O)_4$). This implies that $n \geq 3$ clusters are of the type Ady-$H^+(H_2O)_n$, in which the Ady radical is attached to the surface of a $H^+(H_2O)_n$ cluster. The hydration-size dependent ICPT at the critical cluster size $n_c = 3$ is consistent with the PA values of $(H_2O)_n$ and Ady, as well as the calculated bond dissociation energies for the $Ad^+ + (H_2O)_n$ and Ady + $H^+(H_2O)_n$ dissociation channels. It is also experimentally confirmed by the detection of the $H_7O_3^+$ ion in the CID spectrum of $[Ad(H_2O)_3]^+$ and the good agreement between experimental and computed frequencies for the relevant low-frequency modes describing the proton transfer coordinates ($\nu_{CH···O/OH···C}$) in the fingerprint range.

In general, ionization of alkanes activates one of the C–H bonds and increases its reactivity. For linear alkanes, the reactivity decreases with the length of the alkane chain because of increasing charge delocalization which stabilizes the alkane$^+$ radical cation. With respect to their reactivity towards water, CH_4^+ exhibits ICPT already at $n_c = 1$ leading to $CH_3···H_3O^+$, while pentane$^+$ is less reactive and has a shared proton bond at $n = 1$ and complete ICPT at $n_c = 2$.[78] As the Ad^+ cation is still larger, it is less reactive and thus it requires one more H_2O ligand to produce the shared-proton structure and complete ICPT at $n = 2$ and $n_c = 3$, respectively. Overall, the CH acidity of Ad^+ is higher than that of aromatic (polycyclic) hydrocarbon ions such as benzene$^+$ ($n_c = 4$)[56] and naphthalene$^+$ ($n_c \gg 5$)[35] but more similar to the OH acidity of phenol$^+$ ($n_c = 3$).[78,86]

The ICPT process described herein is the basis for the functionalization of Ad and other diamondoids in polar solvents *via* a radical cation mechanism. This work will be extended in several directions. Currently, IRPD experiments are performed for microhydrated clusters of diamantane$^+$ ($C_{14}H_{20}^+$, Dia$^+$) and substituted Ad^+ ions to investigate the dependence of ICPT on the size and functional groups of the diamondoid cation. In general, a higher n_c value is expected for ICPT of larger diamondoid cations due to reduced CH acidity and charge delocalization.[87] These studies will extend our previous work on microhydrated (protonated) amantadine clusters, in which H_2O ligands bind to the less acidic NH_2^+ (NH_3^+) groups *via* NH···O H-bonds without exhibiting ICPT.[29,59] Further directions include variations of the solvent molecules (*e.g.*, methanol and acetonitrile) and probing the ICPT by electronic spectroscopy.[86,88,89]

Conflicts of interest

There are no conflicts of interest to declare.

Acknowledgements

This study was supported by Deutsche Forschungsgemeinschaft (DO 729/8). The authors acknowledge support of P. Rubli and D. Arildii in recording the fingerprint spectra. We acknowledge fruitful discussions with P. R. Schreiner (Giessen) concerning the reactivity of diamondoid radical cations.

References

1 P. V. R. Schleyer, *J. Am. Chem. Soc.*, 1957, **79**, 3292.

2 R. C. Fort and P. V. R. Schleyer, *Chem. Rev.*, 1964, **64**, 277–300.

3 J. E. Dahl, S. G. Liu and R. M. K. Carlson, *Science*, 2003, **299**, 96–99.

4 H. Schwertfeger and P. R. Schreiner, *ChiuZ*, 2010, **44**, 248–253.

5 P. R. Schreiner, L. V. Chernish, P. A. Gunchenko, E. Y. Tikhonchuk, H. Hausmann, M. Serafin, S. Schlecht, J. E. P. Dahl, R. M. K. Carlson and A. A. Fokin, *Nature*, 2011, **477**, 308.

6 H. Schwertfeger, A. A. Fokin and P. R. Schreiner, *Angew. Chem., Int. Ed.*, 2008, **47**, 1022–1036.

7 W. L. Yang, J. D. Fabbri, T. M. Willey, J. R. I. Lee, J. E. Dahl, R. M. K. Carlson, P. R. Schreiner, A. A. Fokin, B. A. Tkachenko and N. A. Fokina, *Science*, 2007, **316**, 1460–1462.

8 A. A. Fokin and P. R. Schreiner, *Chem. Rev.*, 2002, **102**, 1551–1594.

9 L. Wanka, K. Iqbal and P. R. Schreiner, *Chem. Rev.*, 2013, **113**, 3516–3604.

10 J. E. P. Dahl, J. M. Moldowan, Z. Wei, P. A. Lipton, P. Denisevich, R. Gat, S. Liu, P. R. Schreiner and R. M. K. Carlson, *Angew. Chem., Int. Ed.*, 2010, **49**, 9881–9885.

11 J.-Y. Raty and G. Galli, *Nat. Mater.*, 2003, **2**, 792.

12 P. R. Schreiner, N. A. Fokina, B. A. Tkachenko, H. Hausmann, M. Serafin, J. E. P. Dahl, S. Liu, R. M. K. Carlson and A. A. Fokin, *J. Org. Chem.*, 2006, **71**, 6709–6720.

13 Y. Wang, E. Kioupakis, X. Lu, D. Wegner, R. Yamachika, J. E. Dahl, R. M. K. Carlson, S. G. Louie and M. F. Crommie, *Nat. Mater.*, 2008, **7**, 38.

14 L. Landt, K. Klünder, J. E. Dahl, R. M. K. Carlson, T. Möller and C. Bostedt, *Phys. Rev. Lett.*, 2009, **103**, 47402.

15 D. F. Blake, F. Freund, K. F. M. Krishnan, C. J. Echer, R. Shipp, T. E. Bunch, A. G. Tielens, R. J. Lipari, C. J. D. Hetherington and S. Chang, *Nature*, 1988, **332**, 611.

16 O. Pirali, M. Vervloet, J. E. Dahl, R. M. K. Carlson, A. Tielens and J. Oomens, *Astrophys. J.*, 2007, **661**, 919.

17 M. Steglich, F. Huisken, J. E. Dahl, R. M. K. Carlson and T. Henning, *Astrophys. J.*, 2011, **729**, 91.

18 C. W. Bauschlicher Jr, Y. Liu, A. Ricca, A. L. Mattioda and L. J. Allamandola, *Astrophys. J.*, 2007, **671**, 458.

19 R. S. Lewis, E. Anders and B. T. Draine, *Nature*, 1989, **339**, 117.

20 L. J. Allamandola, S. A. Sandford, A. G. Tielens and T. M. Herbst, *Science*, 1993, **260**, 64–66.

21 R. S. Schwab, A. C. England, D. C. Poskanzer and R. R. Young, *JAMA*, 1969, **208**, 1168–1170.

22 B. Reisberg, R. Doody, A. Stöffler, F. Schmitt, S. Ferris and H. J. Möbius, *N. Engl. J. Med.*, 2003, **348**, 1333–1341.

23 W. L. Davies, R. R. Grunert, R. F. Haff, J. W. McGahen, E. M. Neumayer, M. Paulshock, J. C. Watts, T. R. Wood, E. C. Hermann and C. E. Hoffmann, *Science*, 1964, **144**, 862–863.

24 G. Hubsher, M. Haider and M. S. Okun, *Neurology*, 2012, **78**, 1096–1099.

25 K. Spilovska, F. Zemek, J. Korabecny, E. Nepovimova, O. Soukup, M. Windisch and K. Kuca, *Curr. Med. Chem.*, 2016, **23**, 3245–3266.

26 A. A. Spasov, T. V. Khamidova, L. I. Bugaeva and I. S. Morozov, *Pharm. Chem. J.*, 2000, **34**, 1–7.

27 A. A. Fokin, P. R. Schreiner, P. A. Gunchenko, S. A. Peleshanko, T. Y. E. Shubina, S. D. Isaev, P. V. Tarasenko, N. I. Kulik, H.-M. Schiebel and A. G. Yurchenko, *J. Am. Chem. Soc.*, 2000, **122**, 7317–7326.

28 M. Mella, M. Freccero, T. Soldi, E. Fasani and A. Albini, *J. Org. Chem.*, 1996, **61**, 1413–1422.

29 M. A. R. George, F. Buttenberg, M. Förstel and O. Dopfer, *Phys. Chem. Chem. Phys.*, 2020, **22**, 28123–28139.

30 M. A. R. George, M. Förstel and O. Dopfer, *Angew. Chem., Int. Ed.*, 2020, 12098–12104.

31 O. Dopfer, *Z. Phys. Chem.*, 2005, **219**, 125–168.

32 N. Solcà and O. Dopfer, *Chem. Phys. Lett.*, 2001, **347**, 59–64.

33 N. Solcà and O. Dopfer, *Chem. – Eur. J.*, 2003, **9**, 3154–3161.

34 H.-S. Andrei, N. Solca and O. Dopfer, *ChemPhysChem.*, 2006, **7**, 107–110.

35 K. Chatterjee and O. Dopfer, *Chem. Sci.*, 2018, **9**, 2301–2318.

36 J. Klyne, M. Schmies, M. Fujii and O. Dopfer, *J. Phys. Chem. B*, 2015, **119**, 1388–1406.

37 J. Klyne, M. Schmies, M. Miyazaki, M. Fujii and O. Dopfer, *Phys. Chem. Chem. Phys.*, 2018, **20**, 3148–3164.

38 M. Schütz, Y. Matsumoto, A. Bouchet, M. Öztürk and O. Dopfer, *Phys. Chem. Chem. Phys.*, 2017, **19**, 3970–3986.

39 M. Schmies, M. Miyazaki, M. Fujii and O. Dopfer, *J. Chem. Phys.*, 2014, **141**, 214301.

40 A. Patzer, M. Schütz, T. Möller and O. Dopfer, *Angew. Chem., Int. Ed.*, 2012, **51**, 4925–4929.

41 A. Gali, T. Demján, M. Vörös, G. Thiering, E. Cannuccia and A. Marini, *Nat. Commun.*, 2016, **7**, 1–9.

42 T. Xiong, R. Włodarczyk, L. Gallandi, T. Körzdörfer and P. Saalfrank, *J. Chem. Phys.*, 2018, **148**, 44310.

43 R. T. Bailey, *Spectrochim. Acta, Part A*, 1971, **27**, 1447–1453.

44 O. Pirali, V. Boudon, J. Oomens and M. Vervloet, *J. Chem. Phys.*, 2012, **136**, 24310.

45 J. O. Jensen, *Spectrochim. Acta, Part A*, 2004, **60**, 1895–1905.

46 T. E. Jenkins and J. Lewis, *Spectrochim. Acta, Part A*, 1980, **36**, 259–264.

47 J. W. Raymonda, *J. Chem. Phys.*, 1972, **56**, 3912–3920.

48 S. D. Worley, G. D. Mateescu, C. W. McFarland, R. C. Fort and C. F. Sheley, *J. Am. Chem. Soc.*, 1973, **95**, 7580–7586.

49 S. X. Tian, N. Kishimoto and K. Ohno, *J. Phys. Chem. A*, 2002, **106**, 6541–6553.

50 T. Rander, M. Staiger, R. Richter, T. Zimmermann, L. Landt, D. Wolter, J. E. Dahl, R. M. K. Carlson, B. A. Tkachenko and N. A. Fokina, *J. Chem. Phys.*, 2013, **138**, 24310.

51 A. Candian, J. Bouwman, P. Hemberger, A. Bodi and G. G. M. Tielens Alexander, *Phys. Chem. Chem. Phys.*, 2018, **20**, 5399–5406.

52 P. B. Crandall, D. Müller, J. Leroux, M. Förstel and O. Dopfer, *Astrophys. J.*, 2020, **900**, L20.

53 E. P. L. Hunter and S. G. Lias, *J. Phys. Chem. Ref. Data*, 1998, **27**, 413–656.

54 D. J. Goebbert and P. G. Wenthold, *Eur. J. Mass Spectrom.*, 2004, **10**, 837–845.

55 A. Courty, M. Mons, J. Le Calve, F. Piuzzi and I. Dimicoli, *J. Phys. Chem. A*, 1997, **101**, 1445–1450.

56 M. Miyazaki, A. Fujii, T. Ebata and N. Mikami, *Chem. Phys. Lett.*, 2004, **399**, 412–416.

57 R. Knochenmuss, *Chem. Phys. Lett.*, 1988, **144**, 317.

58 O. Dopfer, *Int. Rev. Phys. Chem.*, 2003, **22**, 437–495.

59 M. A. R. George and O. Dopfer, *Phys. Chem. Chem. Phys.*, 2023, **25**, 5529–5549.

60 P. J. Linstrom and W. G. Mallard, *NIST Chemistry WebBook, NIST Standards and Technology*, Gaithersburg, MD, p. 20889, **http://webbook.nist.gov**, (accessed 2022-09-01).

61 E. D. Glendening, A. E. Reed, J. E. Carpenter and F. Weinhold, *NBO Version 3.1*, 2001.

62 A. E. Reed, L. A. Curtiss and F. Weinhold, *Chem. Rev.*, 1988, **88**, 899–926.

63 T. Shimanouchi, *Tables of Molecular Vibrational Frequencies Consolidated Volume I*, National Bureau of Standards, Washington, DC, 1972, pp. 1–160.

64 F. Huisken, M. Kaloudis and A. Kulcke, *J. Chem. Phys.*, 1996, **104**, 17–25.

65 E. Vogt and H. G. Kjaergaard, *Annu. Rev. Phys. Chem.*, 2022, **73**, 209–231.

66 T. Sawamura, A. Fujii, S. Sato, T. Ebata and N. Mikami, *J. Phys. Chem.*, 1996, **100**, 8131–8138.

67 L. Chen, Z. Ma and J. A. Fournier, *J. Chem. Phys.*, 2022, **157**, 154308.

68 K. Chatterjee and O. Dopfer, *J. Chem. Phys. A*, 2020, **124**, 1134–1151.

69 K. Chatterjee and O. Dopfer, *J. Phys. Chem. A*, 2019, **123**, 7637–7650.

70 K. Chatterjee and O. Dopfer, *Phys. Chem. Chem. Phys.*, 2019, **21**, 25226–25246.

71 J. R. Roscioli, L. R. McCunn and M. A. Johnson, *Science*, 2007, **316**, 249–254.

72 T. Xiong and P. Saalfrank, *J. Phys. Chem. A*, 2019, **123**, 8871–8880.

73 J. Klyne, M. Miyazaki, M. Fujii and O. Dopfer, *Phys. Chem. Chem. Phys.*, 2018, **20**, 3092–3108.

74 K. Chatterjee and O. Dopfer, *Phys. Chem. Chem. Phys.*, 2017, **19**, 32262–32271.

75 E. S. Kryachko and M. T. Nguyen, *J. Phys. Chem. A*, 2001, **105**, 153–155.

76 T. C. Cheng, B. Bandyopadhyay, J. D. Mosley and M. A. Duncan, *J. Am. Chem. Soc.*, 2012, **134**, 13046–13055.

77 D. Bing, T. Hamashima, C.-W. Tsai, A. Fujii and J.-L. Kuo, *Chem. Phys.*, 2013, **421**, 1–9.

78 T. Endo, Y. Matsuda and A. Fujii, *J. Phys. Chem. Lett.*, 2017, **8**, 4716–4719.

79 M. Xie, Y. Matsuda and A. Fujii, *J. Chem. Phys. A*, 2016, **120**, 6351–6356.

80 H. J. Yi, Y. S. Kim, C. J. Choi and K.-H. Jung, *J. Mass Spectrom.*, 1998, **33**, 599–606.

81 A. Ding, R. A. Cassidy, J. H. Futrell and L. Cordis, *J. Phys. Chem.*, 1987, **91**, 2562–2568.

82 N. Solcà and O. Dopfer, *J. Chem. Phys. A*, 2003, **107**, 4046–4055.

83 M. Miyazaki, A. Fujii, T. Ebata and N. Mikami, *Chem. Phys. Lett.*, 2001, **349**, 431–436.

84 M. Miyazaki, A. Fujii, T. Ebata and N. Mikami, *J. Chem. Phys. A*, 2004, **108**, 10656–10660.

85 M. Shimizu, E. Yamashita, M. Mitani and Y. Yoshioka, *Chem. Phys. Lett.*, 2006, **432**, 22–26.

86 S. Sato and N. Mikami, *J. Phys. Chem.*, 1996, **100**, 4765–4769.

87 P. B. Crandall, R. Radloff, M. Förstel and O. Dopfer, *Astrophys. J.*, 2022, **940**, 104.

88 I. Alata, M. Broquier, C. Dedonder-Lardeux, C. Jouvet, M. Kim, W. Y. Sohn, S.-S. Kim, H. Kang, M. Schütz and A. Patzer, *J. Chem. Phys.*, 2011, **134**, 74307.

89 O. Dopfer, A. Patzer, S. Chakraborty, I. Alata, R. Omidyan, M. Broquier, C. Dedonder and C. Jouvet, *J. Chem. Phys.*, 2014, **140**, 124314.